APPENDIX L

Final Report

Improved characterization of reclamation outcomes through the synergistic combination of no-cost satellite data and 3D point clouds: a machine learning approach

OSMRE Cooperative Agreement Number:
035473OSMRE project S23AC00042-00
Final Report

Reporting Period (Jan 2023, Dec 2025)

Principal Author(s):
Randolph H. Wynne[1]., Valerie A. Thomas[1]., Daniel J. Putnam[1].,
Patricia F. Donovan[2]., Carl E. Zipper[2]., W. Lee Daniels[2]

Date Report was Issued (April 2026)

[1]Department of Forest Resources and Environmental Conservation, Virginia Tech, Blacksburg, Virginia, United States
[2]School of Plant and Environmental Sciences, Virginia Tech, Blacksburg, Virginia, United States

Disclaimer

This report was prepared as an account of work sponsored by an agency of the United States Government. Neither the United States Government nor any agency thereof, nor any of their employees, makes any warranty, express or implied, or assumes any legal liability or responsibility for the accuracy, completeness, or usefulness of any information, apparatus, product, or process disclosed, or represents that its use would not infringe privately owned rights. Reference herein to any specific commercial product, process, or service by trade name, trademark, manufacturer, or otherwise does not necessarily constitute or imply its endorsement, recommendation, or favoring by the United States Government or any agency thereof. The views and opinions of authors expressed herein do not necessarily state or reflect those of the United States Government or any agency thereof.

Abstract

Surface mining is a major driver of land cover change in Central Appalachia, often leading to the proliferation of invasive species like autumn olive (*Elaeagnus umbellata*). Accurate tracking of land cover is critical for evaluating reclamation success and monitoring management interventions. This work introduces a novel classification framework integrating multi-source remote sensing data, including Sentinel-2 spectral imagery, phenological and disturbance history metrics from Continuous Change Detection and Classification (CCDC), and the 3D Elevation Program (3DEP) LiDAR structural attributes. A one-vs-rest trained random forest classifier was used to map seven land cover classes across Virginia and Tennessee for the period 2018–2021. The classification achieved area-weighted overall accuracies ranging from 74.3% to 76.8%, generally remaining consistent across previous years and new regions. Results show that autumn olive occupies approximately 9.8% of mined land in Virginia, with its prevalence peaking on sites 14 to 16 years after disturbance before declining as forest cover increases. Conversely, autumn olive remains rare on Tennessee mines, which are dominated by herbaceous and coniferous forest cover. Feature importance analysis showed that while spring spectral composites are the strongest predictors, the addition of LiDAR structural metrics aid in discriminating invasive shrubs from spectrally similar classes. These findings indicate that while revegetation after mining is common, a significant portion of mines remain occupied by invasives. This multi-source approach provides a spatially and temporally stable method for monitoring post-mine land cover composition and for identifying sites where additional management may be needed.

Graphical Materials List

Table of Contents

Disclaimer 2
Abstract 3
Graphical Materials List 3
Introduction 5
Experimental Methods 9
- Study area and land cover samples 9
- Predictor layers 9
- Monthly image composites 9
- Temporal harmonic regression coefficients & temporal trend coefficients 11
- Disturbance history metrics 11
- Structural characteristics 12
- Image mosaicing 12
- Classifier training and evaluation 13
- Land cover analysis 14

Results and Discussion 15
- Classifier accuracy 15
- Land cover proportions 19
- Predictor importance 22
- Discussion 22

Progress on stated hypotheses....29
Conclusion....30
Appendices....38
Appendix A Vegetation indices used....38
Appendix B CCDC and disturbance history metrics....38
Appendix C LiDAR parameters and metrics....38
Appendix D Confusion Matrices for accuracy assessment....39

List of Figures

Figure 1: Land cover samples are distributed across the central Appalachian coal field between the states of Virginia and Tennessee....10
Figure 2: Example CCDC fitted segments and time series breaks....11
Figure 3: Example time series of normalized burn ratio values of an area that has undergone significant land cover change....12
Figure 4: Area-weighted user's and producer's accuracy for each region and year evaluated....16
Figure 5: Area weighted per-class F1 score for each region and year evaluated....17
Figure 6: Overview of predicted land cover maps for the year 2021....19
Figure 7: Per-class area estimates with error bars indicating the 95% confidence interval for each region and year evaluated....20
Figure 8: Chronosequence of land cover proportions by year of mining for mines in Virginia as of 2021....21
Figure 9: Chronosequence of land cover proportions by year of mining for mines in Tennessee as of 2021....21
Figure 10: Normalized (by total) feature importance for all predictors in the trained classifier, categorized into representative groups....22
Figure 11: Scatter plot of model training sample points with two selected predictors from the phenological metrics and LiDAR structural metrics....24
Figure 12: Comparison of predicted maps with varying autumn olive density....25
Figure 13: Two examples of predicted maps with high landscape heterogeneity,....27
Figure 14: Predicted maps with potential overprediction of the shrub/scrub class,....28

List of Tables

Table 1: Land cover class schema, including description and number of training samples from Virginia in 2021....10
Table 2: Class proportions for Virginia 2021 in both mined land cover and the number of validated accuracy assessment samples....14
Table 3: Class proportions for Tennessee 2021 in both mined land cover and the number of validated accuracy assessment samples....14
Table 4: Overall accuracy statistics calculated from post-classification assessment samples for each combination of region and year classified....15
Table 5: Area-weighted user's (UA) and producer's (PA) accuracies with confidence intervals for Virginia maps for each year....18
Table 6: Area-weighted user's (UA) and producer's (PA) accuracies with confidence intervals for Tennessee maps for each year....18
Table 7: Selected flight attributes of the USGS 3DEP LiDAR data used to calculate structural characteristics....39
Table 8: Post-classification accuracy assessment sample confusion matrix for Virginia 2021....39
Table 9: Post-classification accuracy assessment sample confusion matrix for Virginia 2019....40
Table 10: Post-classification accuracy assessment sample confusion matrix for Virginia 2018....40
Table 11: Post-classification accuracy assessment sample confusion matrix for Tennessee 2021....41
Table 12: Post-classification accuracy assessment sample confusion matrix for Tennessee 2019....41

Introduction

The forests of the Appalachian mountains are considered a global biodiversity hotspot (Stein et al., 2000). These valuable natural systems are under threat from surface mining, which has become the dominant form of land cover change in the region (Loveland et al., 2003; Townsend et al., 2009). Surface mining processes involve removing all vegetation, topsoil, and parent material, termed "overburden", before extracting the desired minerals. Surface mining is a general term that encompasses multiple mining methods, including contour, area, highwall, and mountaintop removal (Skousen and Zipper, 2021). These differ from older forms of mining in that they remove the overburden and access the minerals from above to avoid the dangerous enclosed cavities of underground mines. However, these methods lead to a much larger surface area disturbed. Previous work has estimated that surface mines have disturbed over 2.5 million acres in Appalachia and significantly fragmented forest interiors (Wickham et al., 2007; Zipper, 2020).

After a mining company has stopped actively mining, they are required to "reclaim" the land to an equal or better land use than pre-mining (Congress, 1977). This usually involves regrading areas with dangerous topological features like high walls and applying soil amendments to establish vegetation and/or mitigate acid mine drainage. Some mined lands in the region have been reclaimed to forests capable of native succession or "higher or better use" of the land, such as agriculture or development, showing that effective reclamation is possible (Sena et al., 2021; Congress, 1977).

Many mined lands in Appalachia might appear to have successfully reestablished pre-mine vegetation upon evaluation of aerial imagery or in national land cover products. However, invasive plants commonly proliferate on former mines including invasive grasses (*Sericea lespedeza, Festuca arundinacea*), shrubs (*Elaeagnus umbellata, Lonicera maackii*), or trees (*Ailanthus altissima*) (Sena et al., 2021). Many of these invasives were purposefully introduced to Appalachian mines as they are typically drought tolerant and establish cover quickly. However, once these species become dominant on a given site they often out-compete native species for light, space, and nutrients effectively interrupting successional pathways to later successional species (Sena et al., 2021). Specifically, autumn olive (*Elaeagnus umbellata*) is particularly prolific and problematic on former mining sites in the region.

Mapping land cover on mined land is a difficult task as these are typically heterogeneous landscapes and the colonization of invasive species may confound spectral separability, creating inherently mixed pixels. Previous studies have sought to map land cover status of mined land, identifying challenges specific to these highly disturbed areas (Wang et al., 2022; Oo et al., 2022; Szostak et al., 2020; Siljander et al., 2020). Others have conducted small-scale case studies to capture higher spatial or thematic resolution of mined land cover dynamics (Szostak et al., 2020; Siljander et al., 2020; Wang et al., 2022; Oo et al., 2022; Maxwell et al., 2014). However, very few studies specifically identify invasive plants in their land cover classifications. In Oliphant et al. (2017), autumn olive invasion on former surface mines was mapped using Landsat 8 imagery and found it comprised approximately 12.6% of former mines in southwest Virginia. This work exploited autumn olive's distinct annual phenology to aid classification, finding that single-date imagery from early spring and late fall helps differentiate it from other vegetation. In this work, we seek to expand upon Oliphant et al. (2017) to identify autumn olive as well as six other common post-mine land cover types. We also evaluate the efficacy of the classification approach to be applied retrospectively and for other areas outside of southwest Virginia.

Non-native species tend to leaf out and retain their leaves for longer than native species, as Maynard-Bean et al. (2020) found, which can extend the non-native growing season as much as 77 days compared to natives. Recent change detection algorithms for remotely sensed time series data such as breaks for additive seasonal and trend (BFAST) or continuous change detection and classification (CCDC), model intraannual phenology while accounting for interannual change (Verbesselt et al., 2010; Zhu and Woodcock, 2014). These metrics have been used in land cover classification tasks, typically yielding higher accuracy than temporal composites (Xue et al., 2014; Wu et al., 2020; Nguyen et al., 2020). Hartley et al. (2022) differentiated seven different cover classes across West Virginia, finding that harmonic regression coefficients improve classification

accuracy, achieving greater performance than seasonal composites or Global Land Analysis and Discovery (GLAD) phenology metrics. Similarly, Murakami and Tsutsumida (2025) classified six general land cover classes and their transitions globally, they found CCDC harmonic coefficients to outperform BFAST and LandTrendr due to the multidimensional change detection approach implemented in the algorithm. However, there appears to be little research on the applicability of harmonic regression phenology metrics for specifically identifying invasive plants.

While many invasive plants exhibit phenological differentiation, their spectral profiles can still resemble those of non-invasive plants. As identifying a singular species such as autumn olive is a difficult classification task, additional discriminatory power is desired. Light detection and ranging (LiDAR) has been shown to enhance classification accuracy compared to optical imagery for a variety of land cover classification tasks (Sasaki et al., 2012; Zald et al., 2014; Maxwell et al., 2014; Fragoso-Camp´on et al., 2018; Chance et al., 2016). This additional structural information has shown to be beneficial for the identification of invasive shrubs separately from surrounding forests. For Tallow tree *(Triadica sebifera)* and Chinese privet *(Ligustrum sinense)*, the fusion of National Agriculture Imagery Program (NAIP) data and aerial LiDAR reached a maximum accuracy of 87.5% for coastal regions in Alabama and Mississippi (Thapa et al., 2023). Similarly, Choi et al. (2025) found that the addition of LiDAR data improved the detection of common buckthorn *(Rhamnus cathartica)* and bush honeysuckles *(Lonicera spp.)* over high-resolution optical data alone. Additionally, as disturbances facilitate many plant invasions, data describing age and disturbance frequency may improve the identification of these invasions (Kuhman et al., 2010). An added benefit of incorporating long-term time series information is improved temporal consistency in classification, with many national and global land cover products incorporating long-term change detection (Yang et al., 2018; Zhang et al., 2024).

Despite the individual success of harmonic regression, LiDAR, and disturbance tracking in remote sensing, their combined potential for identifying invasive species on reclaimed mines remains underexplored. This work addresses this gap by integrating three complementary data sources and methodologies to enhance autumn olive detection. We propose a novel classification framework that combines harmonic coefficients to isolate the extended growing season, LiDAR metrics to characterize shrub vegetation structure, and time-series derived disturbance metrics to account for site history. This study evaluates the discriminatory power of these combined variables for mapping autumn olive and general post-mining land cover, providing a comprehensive assessment of how multi-source data fusion can improve accuracy and temporal consistency in invasive species monitoring.

Executive Summary

Surface mining is a primary driver of land cover change in Central Appalachia. Accurately tracking land cover transitions is critical for evaluating the success of mine reclamation efforts and monitoring management interventions. A significant challenge across this region is the widespread proliferation of invasive species on former surface mines, particularly autumn olive (*Elaeagnus umbellata*). To address this challenge, the project team successfully developed a novel classification framework with no-cost remotely sensed data designed to map post-mining land cover and specifically identify autumn olive infestations.

During the reporting period, the team designed and trained a one-vs-rest random forest classifier utilizing 1,284 photo-interpreted training sample points collected in Virginia for the year 2021. A major accomplishment of this framework is the synergistic combination of three complementary, no-cost remote sensing data sources. Sentinel-2 monthly surface reflectance composites were utilized, with spring imagery providing the strongest overall predictive power for the model. Inter-annual disturbance history and intra-annual phenological metrics were derived using the Continuous Change Detection and Classification (CCDC) algorithm applied to Landsat and Sentinel-2 time series, respectively. High resolution vertical structure data from the USGS 3D Elevation Program (3DEP) LiDAR was also incorporated. This additional height information was essential for discriminating invasive autumn olive from other vegetation classes with similar spectral and phenological characteristics. This methodology was applied to classify seven land cover types (Barren/developed, Coniferous forest, Deciduous forest, Herbaceous, Autumn olive, Shrub/scrub, and Water) across approximately 12,000 square kilometers in southwestern Virginia and northeastern Tennessee for the years 2018, 2019, and 2021. Additional post-classification stratified validation land cover samples were created for each year and region of land cover maps. These post-classification samples allowed for the calculation of unbiased area-weighted overall and class accuracy metrics to evaluate the temporal and spatial extension of this classification workflow.

The implemented machine learning model proved spatially and temporally stable, demonstrating a promising ability to predict these seven land cover classes in other states within the Appalachian coal fields for retrospective or contemporaneous reclamation monitoring. The model achieved area-weighted overall accuracies ranging from 74.3% to 76.8% across both states and all three evaluated years. The results identified a stark contrast in autumn olive prevalence between the two regions. In Virginia, autumn olive is a significant component of the landscape, occupying approximately 9.8% of the mined land as of 2021. Conversely, the species is rare on Tennessee mines, which are predominantly characterized by herbaceous cover (accounting for 42.2% of the mined area) and coniferous forests. While the classifier successfully identified the most problematic dense and homogenous stands of autumn olive, classification performance degraded in areas with high landscape heterogeneity and varying shrub density. This variability was reflected in individual class accuracy scores (F1 scores), which fluctuated from 0.68 in Virginia to 0.18 in Tennessee. By cross-tabulating land cover proportions with the year of mining, the team established a chronosequence that tracks vegetative reclamation over time. Autumn olive prevalence was shown to peak on sites 14 to 16 years after the last year of mining in Virginia. Following this peak, autumn olive cover proportions decline as native forest cover increases, indicating that while the invasive shrub appears to slow forest establishment, it does not seem to permanently prevent forest establishment over longer timeframes.

The findings generated during this project represent a significant advancement in the ability to monitor complex, highly disturbed environments. The fusion of spectral, temporal, and structural

data provides a robust, stable tool for land managers and regulators to assess post-mine land cover composition accurately. Ultimately, this framework enables the precise identification of sites where targeted management interventions may be necessary to control invasive species and support the successful re-establishment of native forests.

Experimental Methods

Summary: To develop a land cover classification of Appalachian surface mines in the study region, we integrated multi-source remotely sensed data, including Sentinel-2 and Landsat satellite imagery as well as USGS 3D Elevation Program (3DEP) LiDAR to identify seven land cover classes, with an emphasis on invasive autumn olive. Training data consisted of 1,284 photo-interpreted sample points interpreted from high-resolution aerial imagery across Southwestern Virginia. Predictor layers included seasonal spectral composites, harmonic and trend metrics from time series models, and structural attributes from LiDAR. We identified land cover using a one-vs-rest trained random forest classifier for three years (2018 to 2021) and two regions (Virginia and Tennessee). Land cover prediction maps were validated with post-classification stratified samples to obtain unbiased area-weighted measures of accuracy and area estimates with confidence intervals. We summarized post-mining land cover proportions, trends, and their relationship to site age. We also summarized the effectiveness of the spatial and temporal extension of the classification model for regions and years not included in the training data.

Study area and land cover samples

The study area was comprised of the southwest corner of Virginia and the northeast corner of Tennessee encompassing approximately 12,000 km^2 (Figure 1). This region has been extensively mined since the 19th century primarily for coal extraction (Zipper and Skousen, 2021). These two regions fall within the valley and ridge and Appalachian plateau physiographic regions within the central Appalachian Mountains. Historical cover in this region is primarily oak-hickory forests, with significant ecotones resulting from elevation, slope, and aspect gradients (Sena et al., 2021). The forests in this region are also historically disturbance adapted with wildfire being a component of regeneration of many endemic oak and pine species. However, fire suppression, and climate change has been slowly shifting the composition of these forests to more shade-tolerant mesophilic tree species like red maple, American beech, and shrubs like mountain laurel and rhododendron (Abrams, 1992; Alexander et al., 2021).

Land cover points were derived from data used in Oliphant et al. (2017), and supplemental points were added to improve class balance. Each sample point was assigned one of seven land cover categories for three years, 2018, 2019, and 2021 using national agricultural imagery program (NAIP), Virginia base mapping program (VBMP), or Tennessee base mapping program (TBMP) aerial imagery (Table 1) by a single interpreter.

Predictor layers

Monthly image composites

We preprocessed Sentinel-2 data within Google earth engine to remove clouds using the Cloud Score+ product from Google with a clear threshold of 0.5 applied to the 'cs' band and removed snow pixels using the SCL band (Gorelick et al., 2017; Pasquarella et al., 2023). For each year of available land cover data, monthly median composites of Sentinel-2 surface reflectance imagery were calculated using Google earth engine. The composites include several vegetation indices including the normalized difference vegetation index (NDVI, Equation A.1), the two-band enhanced vegetation index (EVI2, Equation A.2), the normalized burn ratio (NBR, Equation A.3), and the normalized burn ratio 2 (NBR2, Equation A.4) (Rouse et al., 1974; Jiang et al., 2008; Key and Benson, 2006). Initially, a multi-band image was created for each month of the year. However, after cloud masking, composite months were limited to March, April, May, June, September, November, and December due to lack of clear pixels in other months.

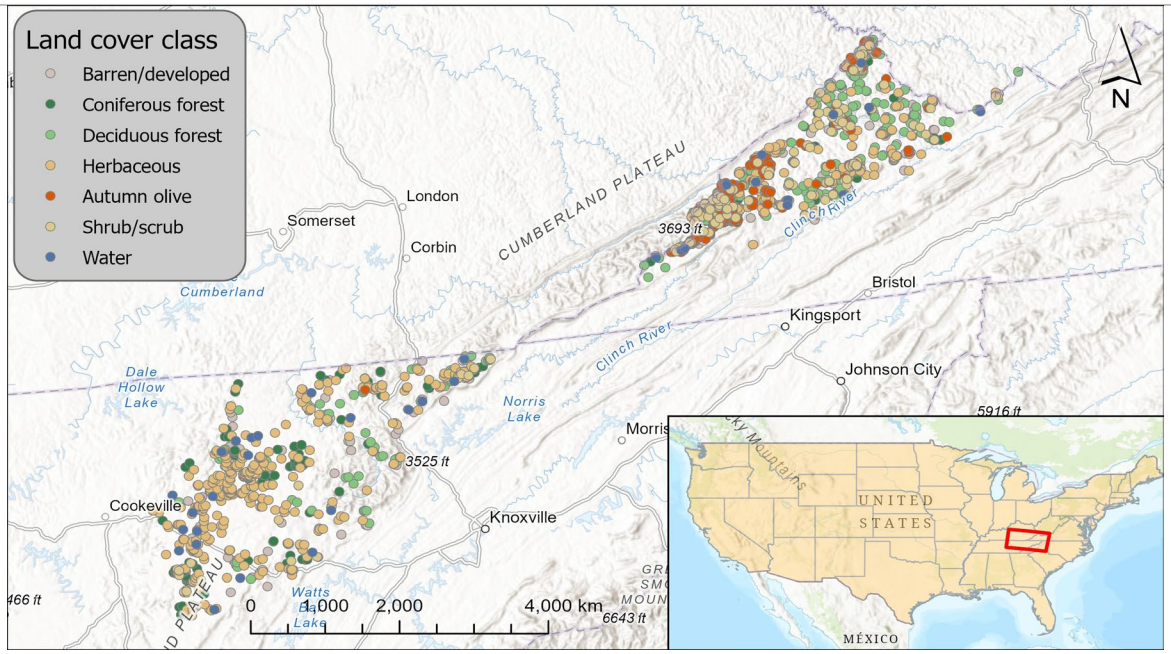


Figure 1: Land cover samples are distributed across the central Appalachian coal field between the states of Virginia and Tennessee.

Table 1: Land cover class schema, including description and number of training samples from Virginia in 2021.

Land cover class	Description	VA 2021 training Samples
Barren/developed	Built-up area, including roads, buildings, processing sites, or areas where vegetation cover is less than 15%	277
Coniferous forest	Forest primarily composed of evergreen trees	79
Deciduous forest	Forest primarily composed of deciduous trees	270
Herbaceous	Non-woody low vegetation including grasses, and some cultivated crops like pasture.	313
Autumn olive	Primarily dominated (>50% cover) by *Elaeagnus umbellata*	204
Shrub/scrub	Woody low vegetation	126
Water	Accumulated pools or flowing water, including tailing ponds	15
TOTAL		1284

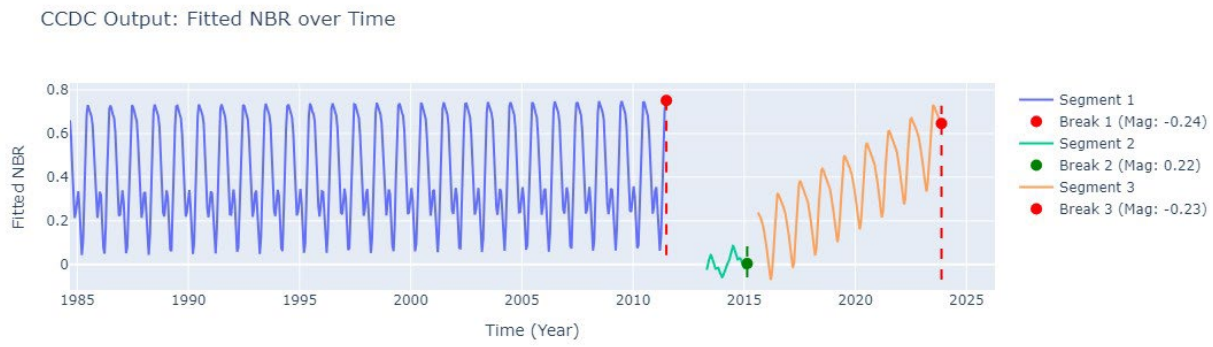


Figure 2: Example CCDC fitted segments and time series breaks.

Temporal harmonic regression coefficients & temporal trend coefficients

The continuous change detection and classification (CCDC) algorithm was used to characterize inter-annual change and intra-annual variation using Sentinel-2 imagery in Google Earth Engine (Figure 2) (Gorelick et al., 2017; Zhu and Woodcock, 2014). These methods have been shown in previous literature to be effective for general land cover classification tasks and that intra-annual variation can be used to differentiate autumn olive from other land cover types (Oliphant et al., 2017; Zhu and Woodcock, 2014). The CCDC algorithm uses all cloud-free images to fit a harmonic regression function with up to 9 parameters for each band in the image and for each homogeneous time segment. The intercept and slope represent inter-annual trends, while Intra-annual variation is represented by the harmonic coefficients, which are fitted to match annual phenology. The representation of intra-annual change in the model are 6 coefficients (three sine, three cosine), but it is common for higher order harmonics to become zero for simple characterization as a result of the model being parameterized through LASSO regularization (Pasquarella et al., 2022). The outputs used in classification include the slope, intercept, RMSE, and all fitted harmonic coefficients for the time segment coinciding with April of the year of classification, as this is when NAIP imagery typically starts acquisitions.

Disturbance history metrics

While CCDC outputs describe inter-annual change within a stationary time segment, they lack information between segments. To characterize long-term disturbance history, a second CCDC output was created based on Landsat time series imagery spanning from 1984 to 2024 (Figure 3). First, we preprocessed the Landsat collection in Google Earth Engine to a uniform set of bands, then masked clouds, cloud shadows, and snow with the QA band. Disturbance history metrics used here were based on Hermosilla et al. (2016) and were meant to produce useful values for both disturbed and stable vegetation pixels to aid classification. Primarily, these metrics record the frequency, duration, and magnitude of change throughout the time series record (more information on metrics are in Appendix A). Metrics used in the classifier include the number of changes in the time series and the average length of time segments. Additionally, the year, magnitude in NBR, and age (relative to classification year) were calculated for both the largest magnitude change and the most recent change before the classification year, the time gap between the largest and most recent change was also calculated.

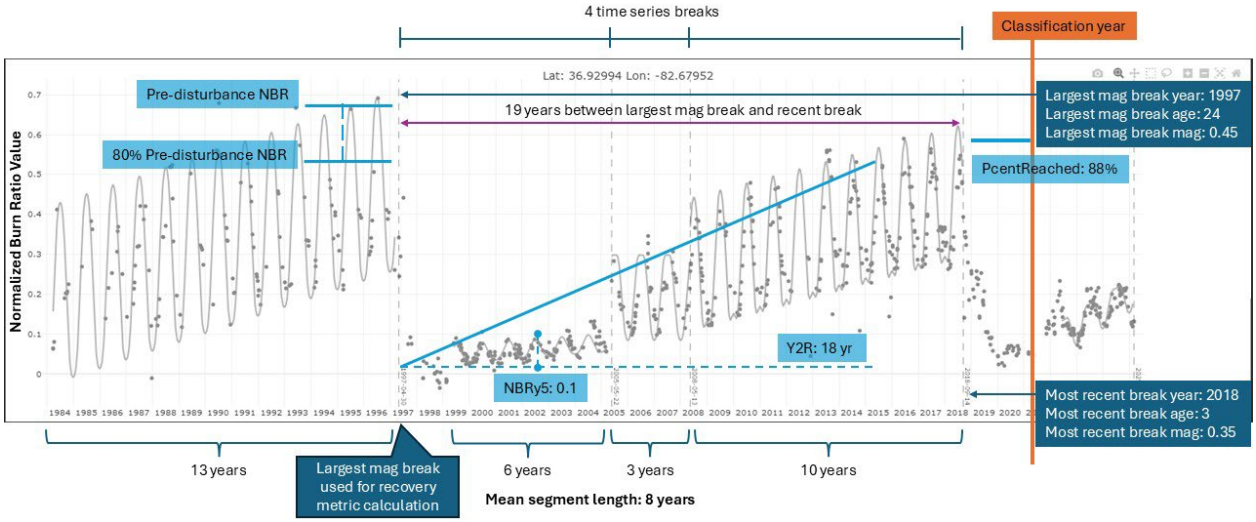


Figure 3: Example time series of normalized burn ratio values of an area that has undergone significant land cover change, including two mining disturbances (1997 and 2018) and revegetation following the first disturbance (2018). Background greyscale points represent all available Landsat observations, curved lines represent CCDC fitted segments. Colored lines and text boxes represent metrics calculated based on the CCDC segment information as well as recovery metrics based on CCDC detected disturbance.

Structural characteristics

USGS 3DEP LiDAR data was used to calculate vegetation structural characteristics. These metrics primarily characterize the height of canopy points, and the vertical distribution of non-ground points above 0.5 m. We obtained the point clouds for two project areas, "Virginia - FEMA R3 South West LiDAR - 2016" collected by a Dewberry subcontractor in winter of 2016-2017, Leading Edge Geomatics, and "TN 27 County QL2 LiDAR (Cumberland Plateau)" collected by Woolpert with two subcontractors in winter of 2015-2016. Both LiDAR acquisitions meet the 3DEP QL2 standards for vertical accuracy (≤ 10 cm), point density (≥ 2 pts/m^2), and nominal point spacing (≤0.71 m) (additional acquisition parameters listed in Appendix C) (Dewberry, 2018; Woolpert, 2015).

While previous studies have utilized a simple digital surface model to aid classification, we hoped to improve land cover differentiation between similar height classes (i.e shrub, autumn olive, and young deciduous) by including additional height metrics typically used in forest growth and inventory models Næsset and Gobakken (2005). The metrics used are similar to those introduced in (Næsset, 2002) and have been widely used in other forest inventory studies (Sheridan et al., 2015; Maxwell et al., 2014). Point cloud metric rasters were created for both study areas using the lidR package in R with a pixel size of 20 m utilizing the multiscale curvature classification algorithm for ground classification and k-nearest neighbors inverse distance weighting algorithm for height normalization (Roussel et al., 2020; Evans and Hudak, 2007). Metrics included in the classification can be summarized as either a direct height measurement (e.g 90th percentile height), a distribution statistic of point heights (e.g standard deviation of heights), or a distribution statistic of lidar returns (e.g standard deviation of first returns).

Image mosaicing

Finally, we accumulated all predictor layers for each year and each region in a local computing environment where we reprojected, resampled, then cropped each predictor layer to the same specifications as the Sentinel-2 composite images which was exported from Google earth engine with a 20 m pixel size. Each image had a nodata value explicitly set to a nodata object for better handling by the classifier and all raster operations were performed using the python API for GDAL. Each region and year combination resulted in an image composed of 256 bands at approximately 38 GB per multiband image.

Classifier training and evaluation

To predict land cover classes from the predictor layers, we used a random forest classifier with a one-vs-rest (OVR) training strategy implemented in Scikit-learn (Pedregosa et al., 2011). The OVR training involves iteratively creating a binary classification problem for each class, separating the "one" target class from the "rest" of the other classes. Each single-class OVR model consists of a random forest with 300 trees, uses balanced class weights to adjust for class imbalance, and is optimized using the log-loss criterion. Each binary classification model is used in prediction ensemble via a majority vote, similar single-class approaches have been suggested in previous studies (Krawczyk et al., 2015; Boyd et al., 2006). We found that this training strategy usefully improved per-class accuracy when evaluating a 30% holdout sample, especially for rarer and easily confused classes like water, shrub/scrub, and barren/developed. All samples in Virginia for the year 2021 were used for model training and prediction of the other years and regions. To understand each predictor's importance in differentiating the land cover classes, we present categorized feature importance values reported in classifier training measured in mean decrease in split impurity (Pedregosa et al., 2011).

We validated the land cover maps according to the latest map accuracy assessment standards and to reduce duplicate and uninformative accuracy statistics such as the Kappa coefficient (Pontius Jr and Millones, 2011; Morales-Barquero et al., 2019; Foody, 2002). Namely, we followed the recommendations from Olofsson et al. (2014) to produce population-scaled (area-weighted) measures of overall, producer's and user's accuracies, as well as the F1 score. These accuracy metrics characterize the error in the classification in different ways, and are based on measures of true positives (TP), true negatives (TN), false positives (FP, also referred to as type 1 error), and false negatives (FN, also referred to as type 2 error). Overall accuracy represents the total number of correct predictions for all classes divided by the number of correct, and incorrect predictions (Eq 2.1). Per-class accuracy metrics of user's and producer's accuracy represent type 1 and type 2 errors, respectively, and are sometimes referred to as precision and recall, respectively (Eqs 2.2, 2.3). Lastly, the F1 score balances the contributions of type 1 and type 2 errors for each class to provide a single value representation of per-class accuracy (Eq 2.4). Each measure was scaled relative to the predicted proportion of each class within the mined area for the respective map area and year by converting the count-based TP, TN, FP, and FN measures from the confusion matrix to hectares. Mapped proportions for the year 2021 and accuracy assessment samples counts are listed in Tables 2 and 3.

$$Overall = \frac{\sum_{j=1}^{k} TP_j + TN_j}{\sum_{j=1}^{k} TP_j + TN_j + FP_j + FN_j} \quad \text{(Eq. 2.1)}$$

$$User's_j = \frac{TP_j}{TP_j + FP_j} \quad \text{(Eq. 2.2)}$$

$$Producer's_j = \frac{TP_j}{TP_j + FN_j} \quad \text{(Eq. 2.3)}$$

$$F1_j = \frac{2 * User's_j + Producer's_j}{User's_j * Producer's_j} \quad \text{(Eq. 2.4)}$$

To determine proportional land cover, the predicted land cover pixel counts were used in the direct stratified estimator, which also allows for estimates of standard error and confidence intervals for the area of each class (Olofsson et al., 2014). To obtain post-classification accuracy assessment points, we used area based proportion stratified random sampling based on 2021 proportions with the `AcATAmA` plugin for QGIS and used the user's accuracies from a 30% hold-out validation to inform class allocation (Liano, 2025; QGIS Development Team, 2024). Additionally, we set the desired standard error to 0.02, the minimum number of samples per class to 50, and set a minimum distance between points of 500 m. These accuracy assessment points were then interpreted following the protocol in section 2.1 for each region and each year. Any validation points falling on truly mixed land cover were not used in the accuracy evaluation. Unfortunately, we were unable to obtain enough high resolution imagery to validate the accuracy assessment points in Tennessee for 2018. Therefore, only validation results for 2021 and 2019 in Tennessee are presented.

Table 2: Class proportions for Virginia 2021 in both mined land cover and the number of validated accuracy assessment samples

Cover Class	VA 2021 Mine Pixel Count	Proportion	Number of validated samples
Barren/developed	182,659	18.9%	109
Coniferous forest	50,989	5.3%	101
Deciduous forest	247,721	25.7%	173
Herbaceous	230,673	23.9%	151
Autumn olive	139,490	14.5%	48
Shrub/scrub	108,097	11.2%	38
Water	5,580	0.6%	33

Table 3: Class proportions for Tennessee 2021 in both mined land cover and the number of validated accuracy assessment samples

Cover Class	TN 2021 Mine Pixel Count	Proportion	Number of validated samples
Barren/developed	72,971	11.5%	98
Coniferous forest	91,149	14.3%	95
Deciduous forest	100,347	15.8%	93
Herbaceous	277,428	43.6%	263
Autumn olive	21,397	3.4%	7
Shrub/scrub	60,521	9.5%	38
Water	13,041	2.0%	39

Land cover analysis

Once land cover prediction maps were created and validated, we tabulated each land cover class on mined land in each region according to the extent and year mined defined by the MTM dataset from SkyTruth using the `Terra` package in R (Thomas, 2023; Hijmans, 2025; R Core Team, 2021). We also cross-tabulated land cover proportions with the year of mining reported by the SkyTruth dataset to understand land cover composition of different site ages. Each year of mine age composition was normalized to show relative proportions for each year of mining.

Results and Discussion

Classifier accuracy

Initial training indicated good model performance with an OOB overall accuracy of 79.0% and a score of 77.0% on a 30% hold-out sample for Virginia in 2021. The classifier appears to be more consistent in temporal transferability compared to spatial transferability when evaluated on a post-classification stratified sample. Overall accuracy from sample counts remains consistent in Virginia through time (78.4% - 79.0%), but falls when predicting in Tennessee (75.2% - 76.5%) (Table 4). However, it appears that when accounting for predominant land cover types in both regions, the classifier remains consistent through space and time, only varying by ≈ 2% in area-weighted accuracy (Table 4). Per-class classifier performance is most consistent for forest classes, herbaceous, and barren/developed with relatively small differences in user's or producer's accuracy between years and regions (Figure 4). Coniferous forest, however, shows much lower producer's accuracy in Virginia for all years, this is likely due to the lower proportion of coniferous forest in Virginia as samplebased producer's accuracy ranges from 69% to 72% (Table 10, 9, 8). The Shrub/scrub class has consistently low accuracy scores and high variance with F1 scores ranging from 0.23 (TN 2019) to 0.43 (VA 2021) (Figure 5). Classifier accuracy for autumn olive is highly variable with F1 scores ranging from 0.18 (TN 2021) to 0.68 (VA 2021). Additionally, autumn olive appears to be underpredicted on the map as the user's accuracies are consistently lower than producer's accuracies (Figure 4). Autumn olive accuracy also exhibits the most temporal variation, with scores in Virginia ranging from 47.0% to 57.1% and 57.1% to 95.2% for user's and producer's accuracy, respectively (Tables 6,5).

Table 4: Overall accuracy statistics calculated from post-classification assessment samples for each combination of region and year classified.

State	Year	Area-weighted overall accuracy	Sample-based overall accuracy	Number of validation samples
VA	2021	74.4% ± 3.5%	79.0%	656
	2019	74.3% ± 3.4%	78.4%	649
	2018	75.5% ± 3.4%	78.9%	649
TN	2021	76.0% ± 3.0%	75.2%	633
	2019	76.8% ± 2.9%	76.5%	630

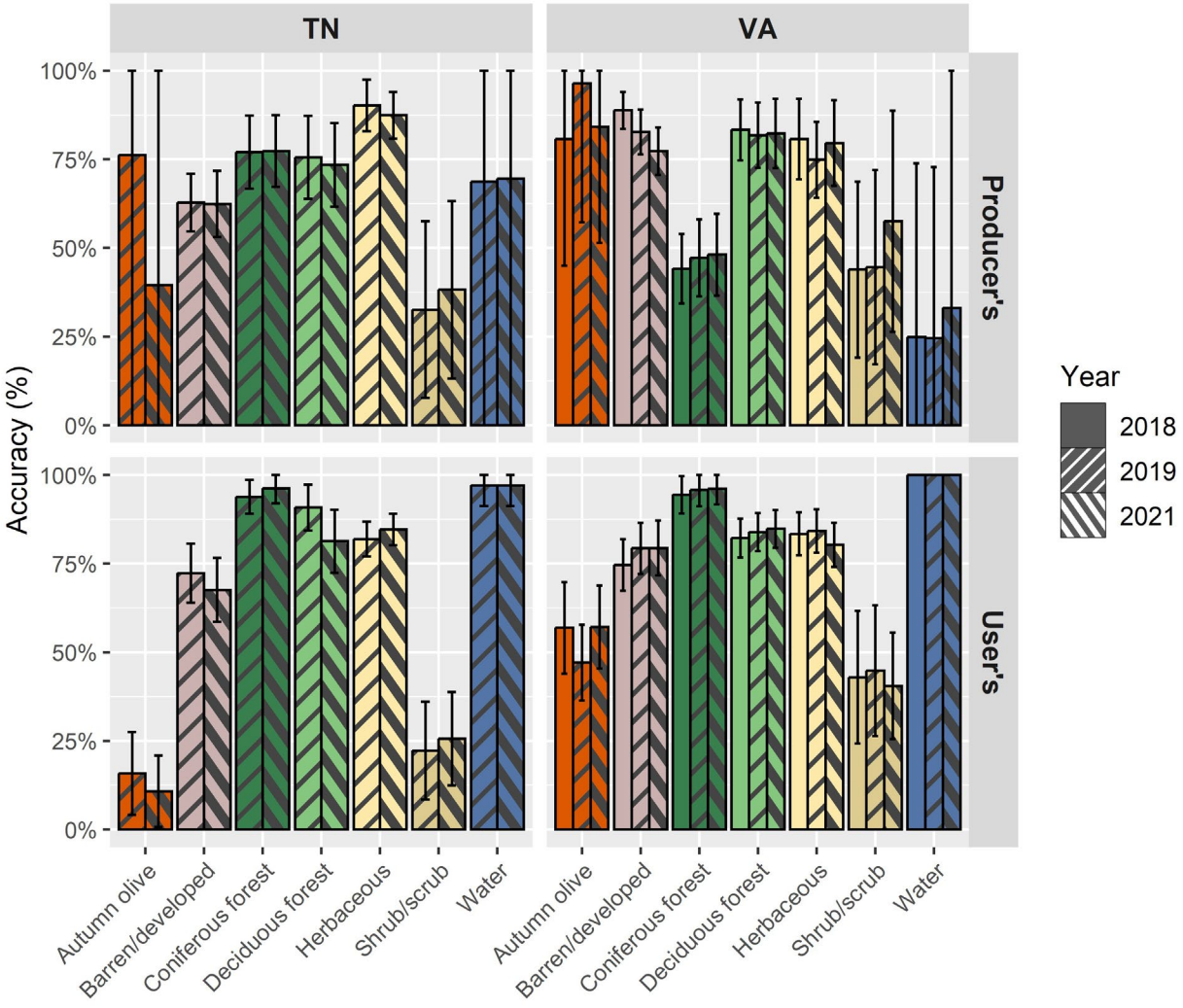


Figure 4: Area-weighted user's and producer's accuracy for each region and year evaluated. Error bars indicate the 95% confidence interval for the accuracy estimate.

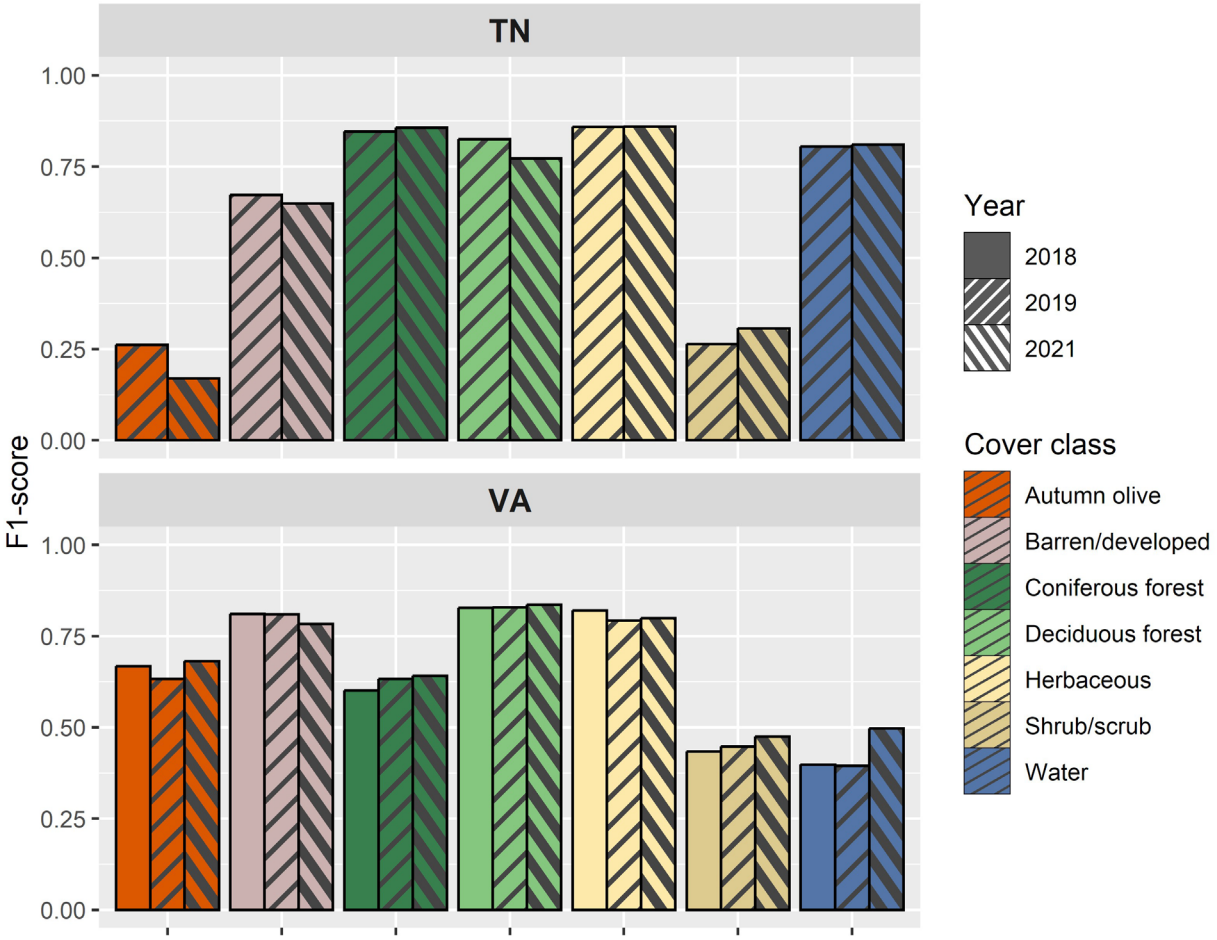


Figure 5: Area weighted per-class F1 score for each region and year evaluated

Table 5: Area-weighted user's (UA) and producer's (PA) accuracies with confidence intervals for Virginia maps for each year.

Cover Class		Virginia 2021	Virginia 2019	Virginia 2018
Barren/developed	UA	79.4% ± 7.7%	79.3% ± 7.2%	74.6% ± 7.3%
	PA	77.3% ± 6.7%	82.7% ± 6.3%	88.8% ± 5.2%
Coniferous forest	UA	96.1% ± 4.4%	95.8% ± 4.7%	94.4% ± 5.3%
	PA	48.1% ± 11.5%	47.2% ± 10.9%	44.1% ± 9.8%
Deciduous forest	UA	84.8% ± 5.3%	83.9% ± 5.4%	82.2% ± 5.5%
	PA	82.3% ± 9.8%	81.8% ± 9.2%	83.3% ± 8.6%
Herbaceous	UA	80.3% ± 6.2%	84.2% ± 6.1%	83.4% ± 6.1%
	PA	79.6% ± 12.1%	74.9% ± 10.7%	80.7% ± 11.4%
Autumn olive	UA	57.1% ± 11.7%	47.1% ± 10.7%	56.9% ± 12.9%
	PA	84.2% ± 32.8%	96.4% ± 39.2%	80.7% ± 35.7%
Shrub/scrub	UA	40.5% ± 15.0%	44.8% ± 18.4%	42.9% ± 18.7%
	PA	57.5% ± 31.2%	44.6% ± 27.4%	43.9% ± 24.8%
Water	UA	100.0% ± 0.0%	100.0% ± 0.0%	100.0% ± 0.0%
	PA	33.1% ± 78.8%	24.6% ± 48.2%	24.9% ± 49.0%

Table 6: Area-weighted user's (UA) and producer's (PA) accuracies with confidence intervals for Tennessee maps for each year.

Cover Class		Tennessee 2021	Tennessee 2019
Barren/developed	UA	67.6% ± 9.0%	72.3% ± 8.3%
	PA	62.4% ± 9.3%	62.8% ± 8.1%
Coniferous forest	UA	96.2% ± 4.2%	93.8% ± 4.8%
	PA	77.3% ± 10.1%	77.0% ± 10.3%
Deciduous forest	UA	81.3% ± 8.9%	90.8% ± 6.5%
	PA	73.4% ± 11.8%	75.5% ± 11.7%
Herbaceous	UA	84.6% ± 4.4%	81.9% ± 4.9%
	PA	87.4% ± 6.6%	90.2% ± 7.3%
Autumn olive	UA	10.8% ± 10.1%	15.8% ± 11.7%
	PA	39.5% ± 149.0%	76.2% ± 320.4%
Shrub/scrub	UA	25.6% ± 13.2%	22.2% ± 13.8%
	PA	38.2% ± 25.0%	32.6% ± 24.9%
Water	UA	97.1% ± 5.8%	97.1% ± 5.8%
	PA	69.5% ± 88.0%	68.7% ± 84.7%

Land cover proportions

Figure 6 shows predicted land cover maps for 2021, including the full mapped area (A) and the land cover within the mining extent identified by Skytruth (B) (Thomas, 2023). The resulting land cover estimates from the classified maps show distinct differences in cover proportion on mines between regions, with subtle differences between years. Most notably, autumn olive represents a very small proportion of the area disturbed by mining in Tennessee, while in Virginia it represents as much as 3,788 ± 1,041 ha or 9.8% ± 2.7% for the year 2021 (Figure 7). Herbaceous cover is by far the most common land cover on mines in Tennessee at an estimated 10,741 ± 709 ha or 42.2% ± 2.8% in 2021, greater than both forest cover types combined. While in Virginia, deciduous forest cover predominates, covering 10,209 ± 761 ha or 26.4% ± 2.0% in 2021, with herbaceous cover second most common.

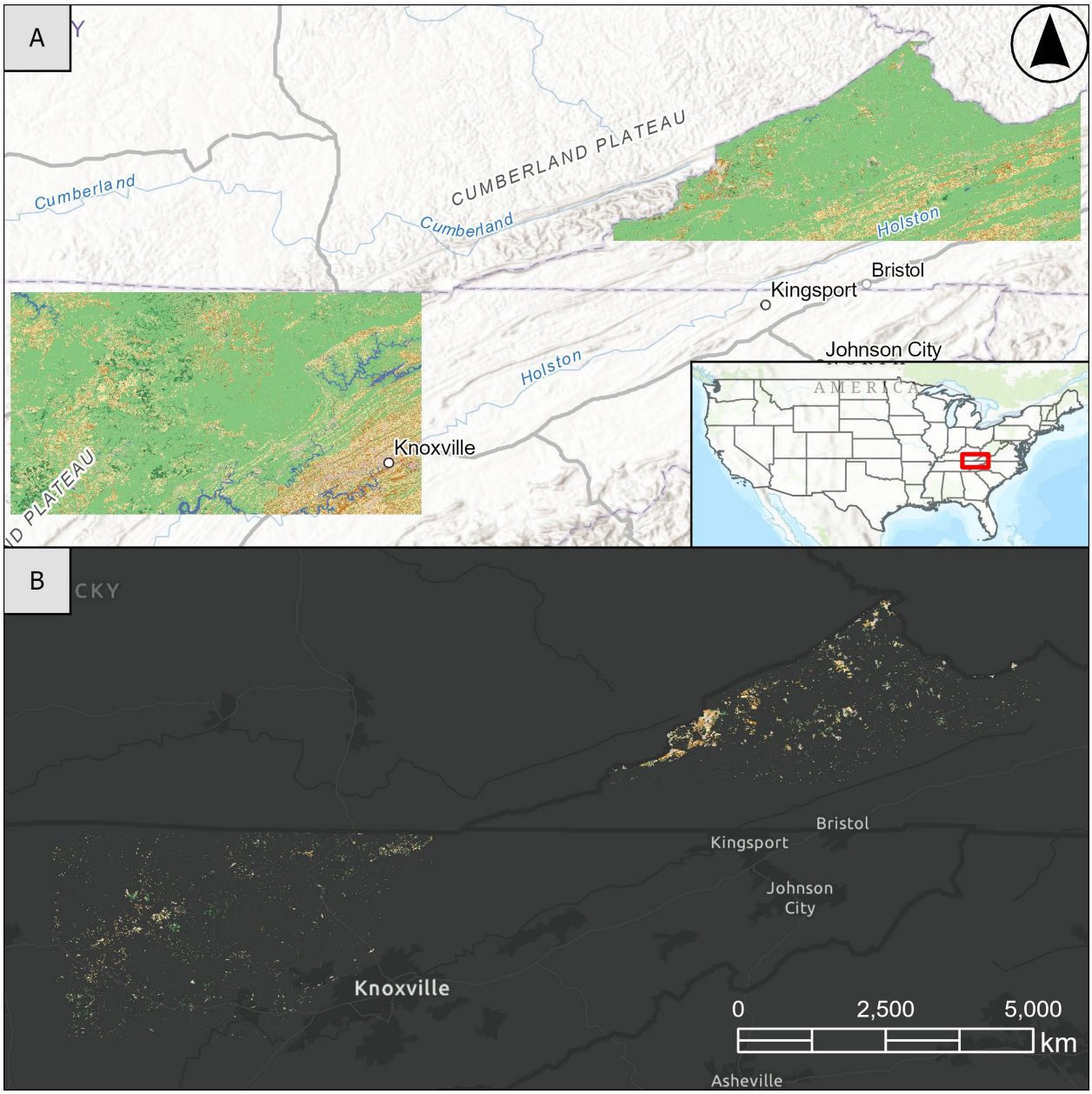


Figure 6: Overview of predicted land cover maps for the year 2021. A: Complete area mapped for land cover prediction in both Virginia and Tennessee. B: Land cover predictions within the historical mining extent identified by Thomas (2023) in Virginia and Tennessee

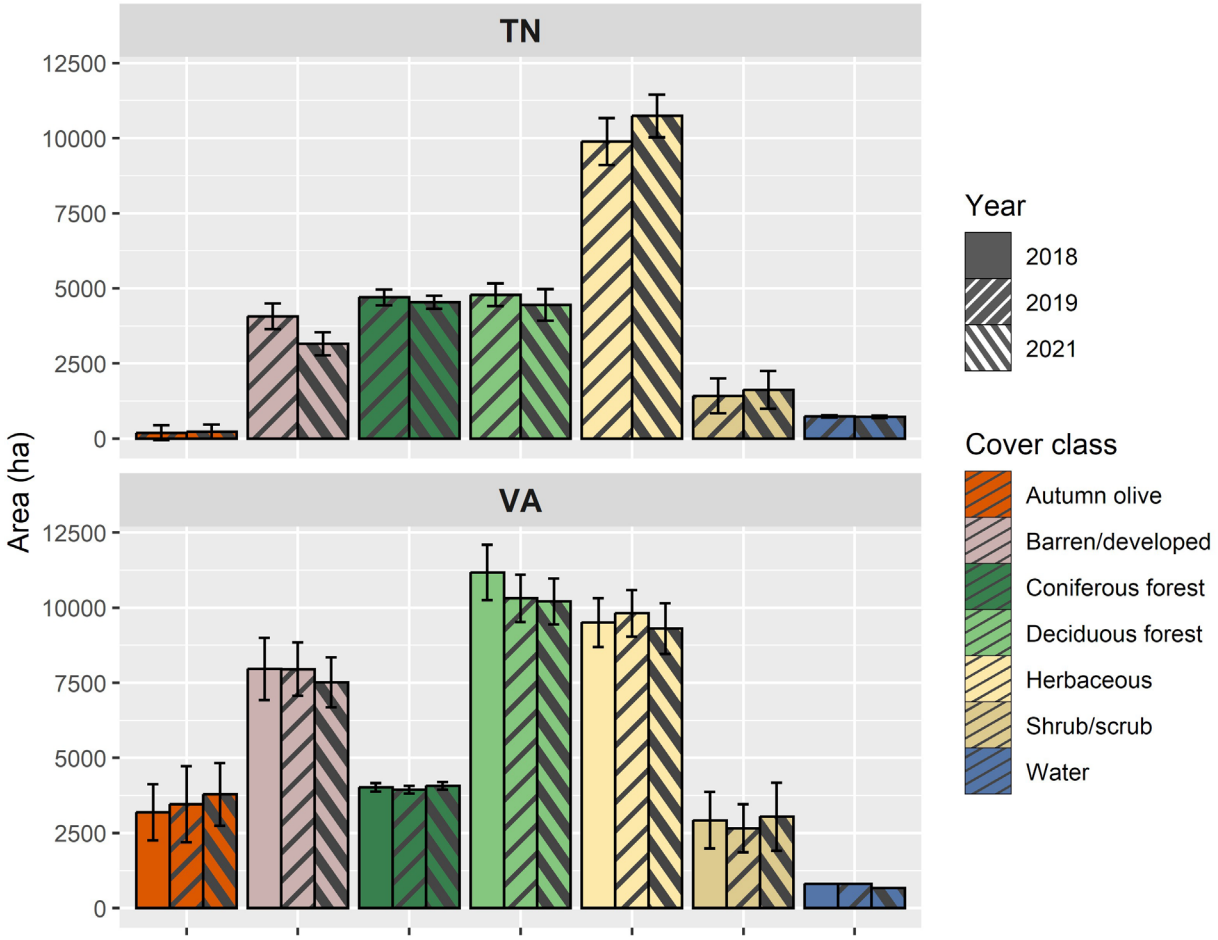


Figure 7: Per-class area estimates with error bars indicating the 95% confidence interval for each region and year evaluated.

As surface mining is a high-intensity land cover disturbance, we should expect to see successional dynamics occurring across a chronosequence of the mapped land cover by mining year. Recently mined sites have high proportions of barren/developed land and herbaceous vegetation, which are replaced through time by forest, shrub, and autumn olive cover (Figures 8, 9). Mines in Virginia decrease in barren/developed proportion from 78.5% in 2021 to 3.3% by 2010, this transition appears slower in Tennessee, decreasing from 67.9% in 2021 to 6.3% by 2010 (Figures 8 9). Autumn olive cover is most prevalent on Virginia mines last active in 2007, accounting for 36.3% of the total area of these mines. However, autumn olive cover proportion decreases to just 8.5% for the oldest mines in Virginia (last active in 1985), suggesting that forest cover is largely able to overtop and outcompete autumn olive across the landscape given enough time (Figure 8). Coniferous forests show an unusual pattern in the chronosequence in Figure 9, with a seemingly anomalous spike in proportion from 2000 to 2007. It is unclear what might be causing this pattern in coniferous forest proportionality, as mining extent is not drastically different in these years compared to other years. We could not determine any geospatial or classification cause for this increase in coniferous forest area.

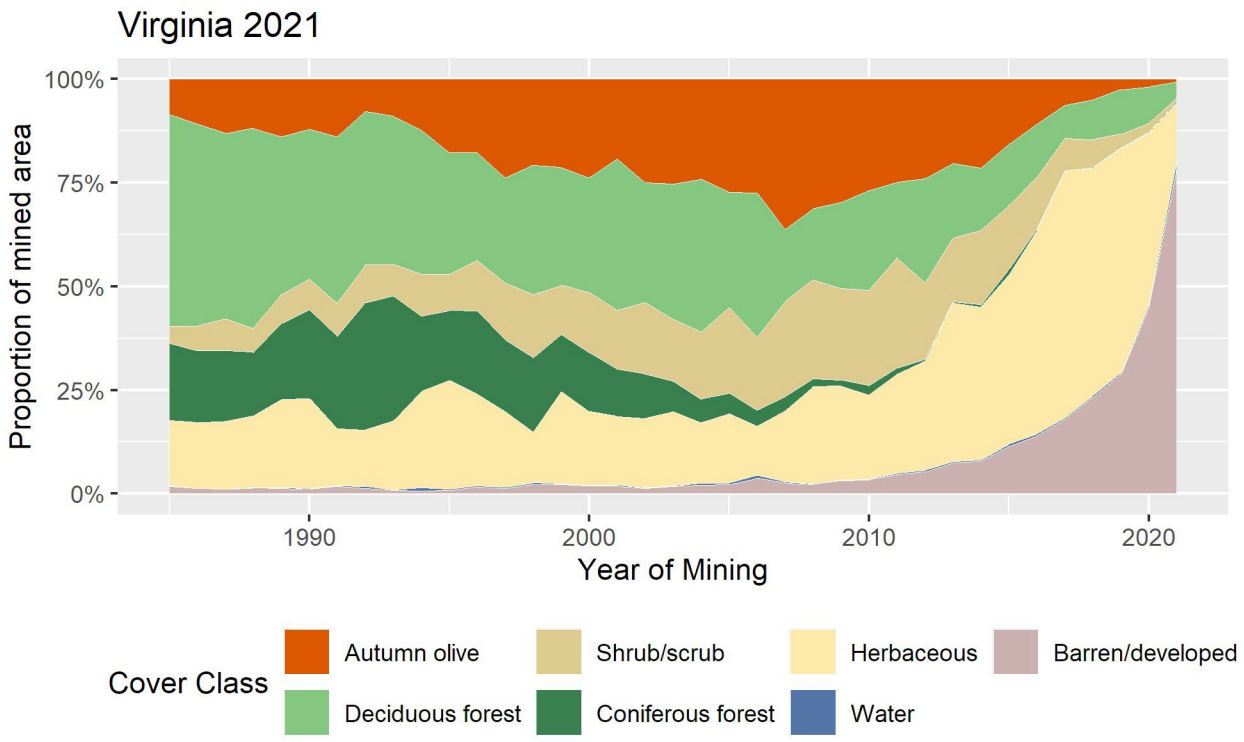


Figure 8: Chronosequence of land cover proportions by year of mining for mines in Virginia as of 2021

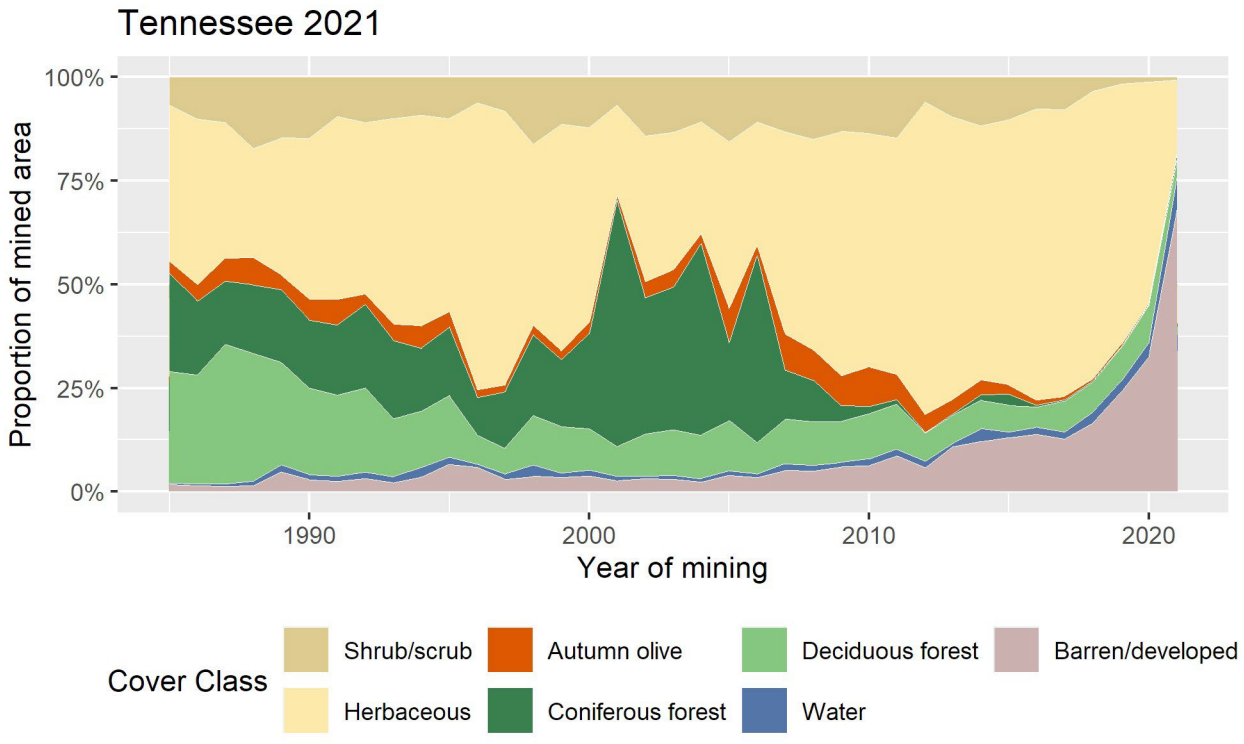


Figure 9: Chronosequence of land cover proportions by year of mining for mines in Tennessee as of 2021

Predictor importance

Importance scores from classifier training indicate that Sentinel-2 monthly composites compose the majority of model importance, of which spring imagery is most important (Figure 10). Interannual change metrics and LiDAR structure are the second and third most important features, respectively. Surprisingly, CCDC intraannual phenology metrics represent the smallest share of feature importance, suggesting that directly classifying spring image composites with interannual change information and height metrics may suffice if a lower dimensional feature space is desired.

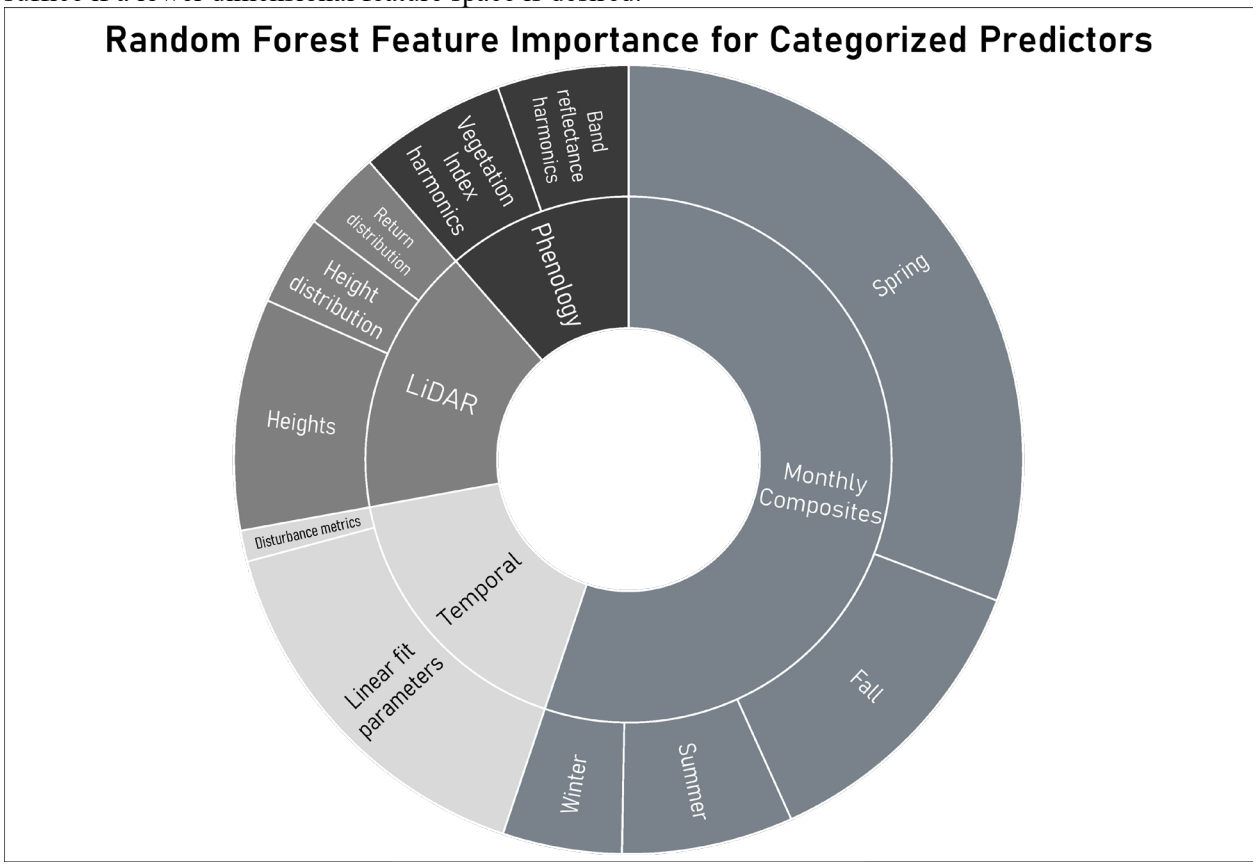


Figure 10: Normalized (by total) feature importance for all predictors in the trained classifier, categorized into representative groups.

Discussion

This work sought to expand upon previous efforts to map land cover in reclaimed Appalachian surface mines by developing a multi-class classification that specifically identifies autumn olive. By integrating Sentinel-2 spectral data and phenology metrics, Landsat derived disturbance, and LiDAR derived structural data, we successfully classified seven land cover types across two states and three years. This work serves as a methodological successor to Oliphant et al. (2017), which first demonstrated the feasibility of mapping autumn olive on these landscapes using Landsat 8. We showed that the current methodology is spatially and temporally extendable, with overall accuracy ranging from 75.2% to 79.0%, but variable across classes. Our main contribution is demonstrating that mapping autumn olive in a multi-class setting is feasible (F1 = 0.68), but it remains challenging, especially in areas where it is uncommon, like Tennessee (F1 = 0.18). Where Oliphant et al. (2017) focused on a binary classification of autumn olive presence/absence, our work advanced this by identifying autumn olive within a broader set of land cover categories. Previous work has noted that binary classifiers generally outperform multi-class problems, which is also the case in comparing these two studies, with Oliphant et al. (2017) achieving an F1 score of 0.82, compared to 0.68 in the current study (Silva et al., 2017). The primary findings of Oliphant et al. (2017) indicated that phenology is key to autumn olive detection, with their study leveraging multi-temporal Landsat 8 images from spring and fall. We expanded this concept by

incorporating CCDC phenological metrics and monthly composites as predictors. Although our results suggest that direct image observations remain the strongest predictors (Figure 10), it is likely the long term temporal information aided in the temporal stability of the overall accuracy, as suggested by previous studies (Wilson et al., 2018; Pasquarella et al., 2018; Pham et al., 2024). The addition of LiDAR-derived structural metrics was intended to solve the very problem Oliphant et al. (2017) noted: separating autumn olive from other vegetation types that may have similar spectral properties but different physical structures. We did not evaluate the amount of introduced errors due to the temporal misalignment of LiDAR and image data, but this misalignment could be responsible for the confusion between herbaceous and autumn olive classes.

Our land cover proportion analysis for Virginia in 2021 estimated autumn olive cover at 9.8% ± 2.7%. This is consistent with the 12.6% reported by Oliphant et al. (2017) for a similar area in 2014. It is unclear if this difference in these two estimates is due to classification or from autumn olive removal during the 2014 to 2021 time frame, which also could have been counteracted by autumn olive expansion. As Oliphant et al. (2017) noted, the last known intentional planting of autumn olive for reclamation in this area was in 2003, so additional area expansion would most likely be due to natural propagation. The chronosequence in Figure8 shows a very similar pattern of the time-dependence of autumn olive presence to results in Oliphant et al. (2017), but the peak of autumn olive presence is about 10 years later (1998 in Oliphant et al. (2017), and 2007 in Figure 8). This suggests that autumn olive is most prolific on mines 14 to 16 years after initial disturbance, after which forest cover becomes more prominent. There is consensus in the literature that autumn olive has the ability to cause "arrested succession", or the interruption of successional pathways through the establishment of monocultural cover (Sena et al., 2021; Cavender et al., 2014; Pritekel et al., 2006). However, few studies have directly observed this phenomenon on reclaimed mines. Observations of reforestation plots four years after reclamation from Evans et al. (2013) showed autumn olive as having five times the volume index of all planted and volunteer trees combined, although plant tree survival was lower than expected. Franke et al. (2018) found that the removal of autumn olive resulted in greater tree survival, but had no significant impact on growth. Finally, in an evaluation of plots across three mine sites in Ohio, Ruggles et al. (2021) found the proportion of invasive plants, including autumn olive, decreased with site age, suggesting that native forest succession was slowed, not stopped. Our results (Figure 8) largely corroborate these findings, suggesting that autumn olive is prolific, negatively impacts forest establishment, but likely does not prevent it given enough time.

To our knowledge, this study is the first integration of phenological metrics, long-term disturbance information, and structural LiDAR metrics for land cover classification. Other studies commonly combine multispectral or hyperspectral imagery with LiDAR or imaging radar to incorporate complementary structural information and have found moderate improvements in accuracy (Fagan et al., 2018; Adams et al., 2020; Xu et al., 2024). We suggest this novel combination of data is essential for identifying specific species of interest on former mines, considering the ever-evolving plant communities on these dynamic landscapes (Sena et al., 2021). Despite the use of multi-source data, the classification of autumn olive remained a significant challenge. The classifier's performance for autumn olive was variable, ranging from an F1 score of 0.68 (VA 2021) to 0.18 (TN 2021). As shown in Figure 12, the model appears to perform well on dense, homogenous stands of autumn olive (Figure 12A,B) but struggles with areas of varying density (Figure 12C,D) and high landscape heterogeneity (Figure 13), often misclassifying as herbaceous, or overpredicting in young forests. A similar limitation related to autumn olive density was noted by Oliphant et al. (2017).

We argue that the current unique combination of data sources represents an advancement in classification approach, which, even when limiting the number of predictors, results in good class discrimination within the feature space. Figure 11 shows that the combination of a phenological metric (first order cosine coefficient of NDVI) and a LiDAR structural metric (proportion of LiDAR returns between 0.5 - 2.5 m) results in high class separability of autumn olive. To improve upon these advances, future work might improve detection capability by directly predicting abundance as in Shiferaw et al. (2019) or by using higher spatial resolution data as in Maxwell et al. (2014).

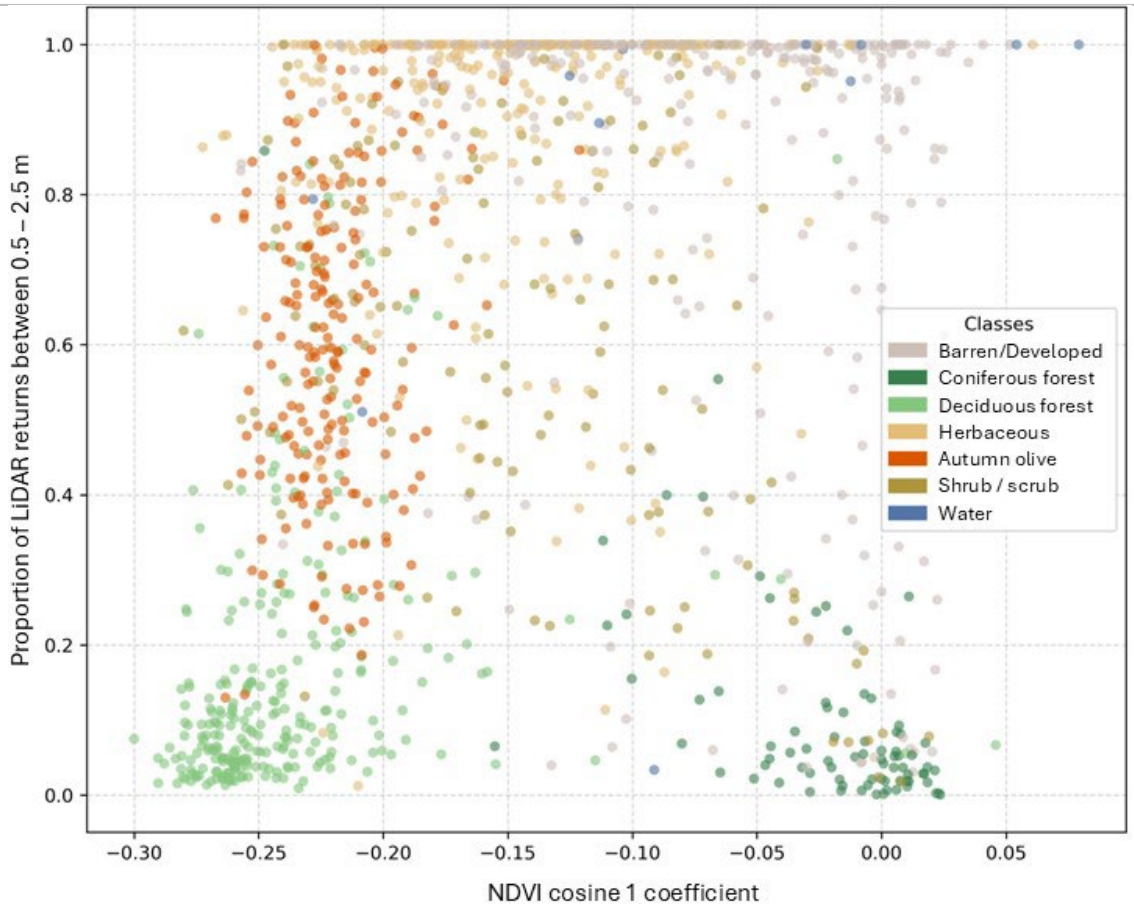


Figure 11: Scatter plot of model training sample points with two selected predictors from the phenological metrics and LiDAR structural metrics. The Y axis is a measure of the vertical distribution of LiDAR height returns, indicating autumn olive heights are uniquely clustered between 0.5 and 2.5 m above ground. The X axis is an estimate of phenology, specifically, the first-order cosine coefficient in the normalized difference vegetation index (NDVI). These two metrics show good class separation in general and help isolate autumn olive samples from spectrally and phenologically similar forest classes (lower proportion of low LiDAR returns) and structurally similar shrub classes (higher NDVI cosine coefficient) within the feature space.

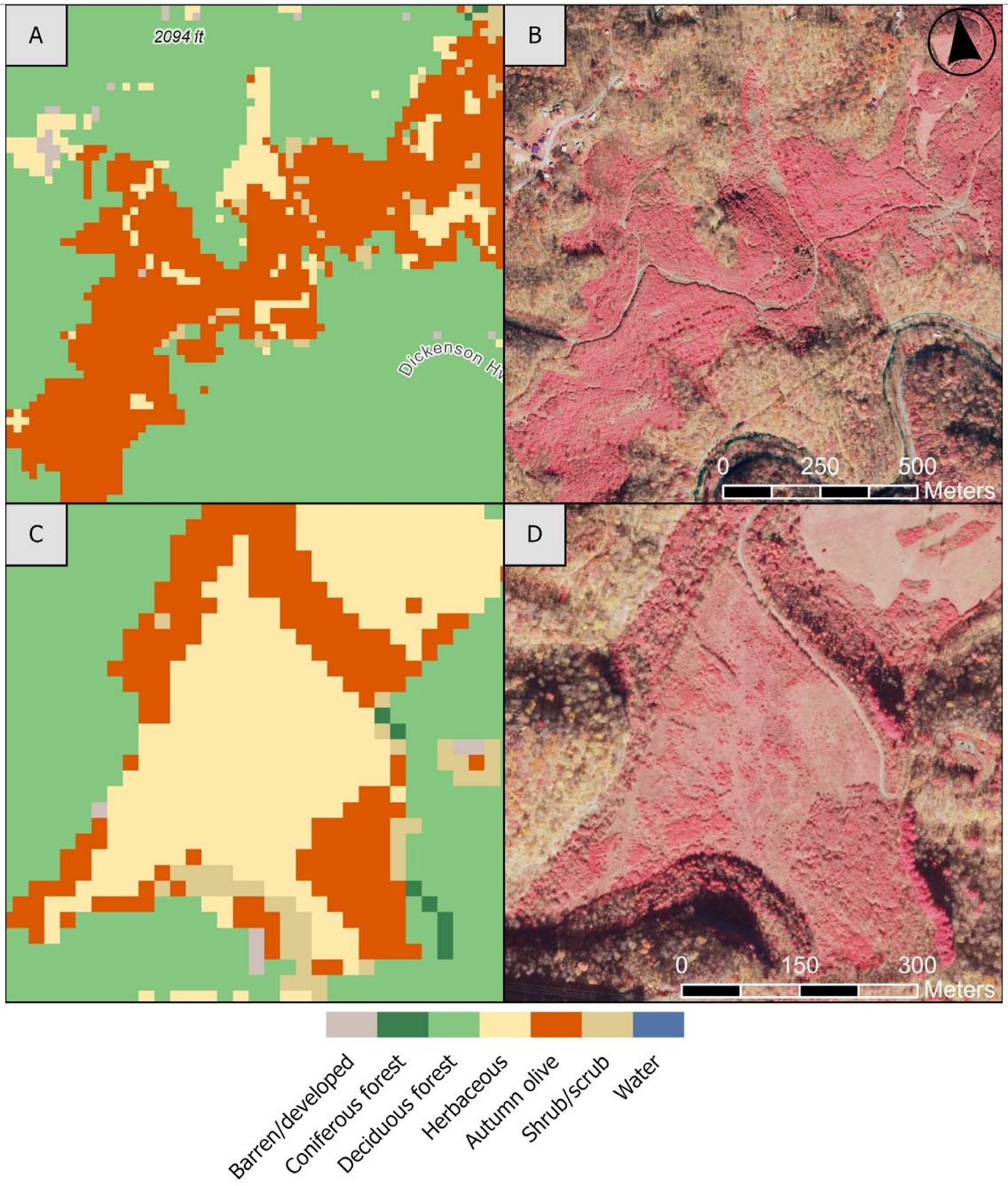


Figure 12: Comparison of predicted maps with varying autumn olive density. A: Classified land cover data of a mine near Clinchco Virginia, almost entirely dense autumn olive. B: False color NAIP aerial image of A. C: Classified land cover data of a mine near Coeburn Virginia, majority of vegetation is autumn olive, but with varying density. D: False color NAIP aerial imagery of C.

Surface mining disturbs landscapes at a fundamental level, creating soil and topographic conditions that are highly variable over short distances. Our results visually demonstrate this fragmentation; for example, the predicted maps in Figure 13 show a "salt and pepper" distribution of classes that mirrors the spatial variance seen in the corresponding NAIP imagery. This heterogeneity is not merely a classification artifact but a reflection of the variability inherent to these landscapes (Chen et al., 2018). Recent evaluations of global 10 m land cover products corroborate this, demonstrating that classification accuracy consistently degrades in fragmented and spatially heterogeneous landscapes (Xu et al., 2024). Additionally, studies like Maxwell et al. (2014) and Szostak et al. (2020) have highlighted that while including texture or structural metrics can improve accuracy, the fundamental spatial resolution of satellite imagery likely limits the ability to classify early successional mine vegetation effectively. Our confusion matrices (Appendix D) reflect this, showing significant misclassification between Barren/developed, Herbaceous, and Shrub/scrub classes. This suggests that in highly heterogeneous mine landscapes, these classes exist on a continuum rather than as discrete categories, making hard boundaries difficult to define at this spatial scale.

Issues of landscape heterogeneity, spatial scale, and thematic class definitions are strongly exhibited in the shrub/scrub class, which showed the lowest validation accuracy of any class (Figure 4). This class, inspired by the definition in the Anderson Level II classification system, is distinguished thematically by its low canopy height from forest classes (Anderson et al., 1976). As seen in Figure 14, shrub/scrub is often overpredicted in areas that should likely be classified as forest or herbaceous, which is also reflected in the confusion matrices in Appendix D. Previous classifications of mined land such as Szostak et al. (2020) have instead defined this class as "transitional woodland." They also found this to be the most difficult class to identify with user's accuracy between 61% and 90% when using similar image data to the current study (Szostak et al., 2020). The identification of this class is potentially quite valuable from a land management perspective, as it explicitly highlights land on a thematic boundary between low vegetation and established forests. These are areas that could benefit the most from management interventions to encourage the establishment of native forests.

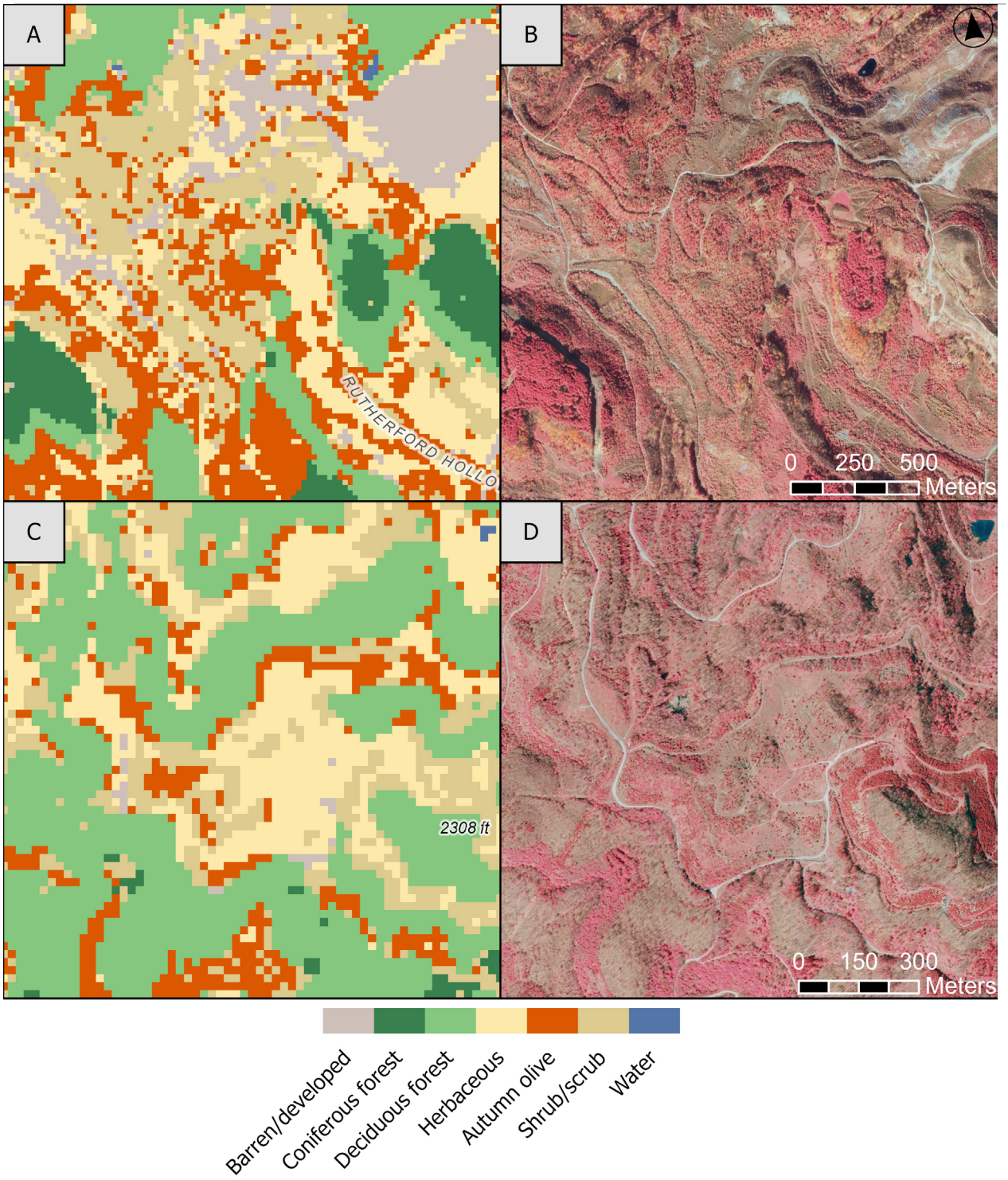


Figure 13: Two examples of predicted maps with high landscape heterogeneity, A: Classified land cover data of a mine near Appalachia Virginia B: False color NAIP aerial imagery of A. C: Classified land cover data of a mine near Duff Tennessee. D: False color NAIP aerial imagery of C.

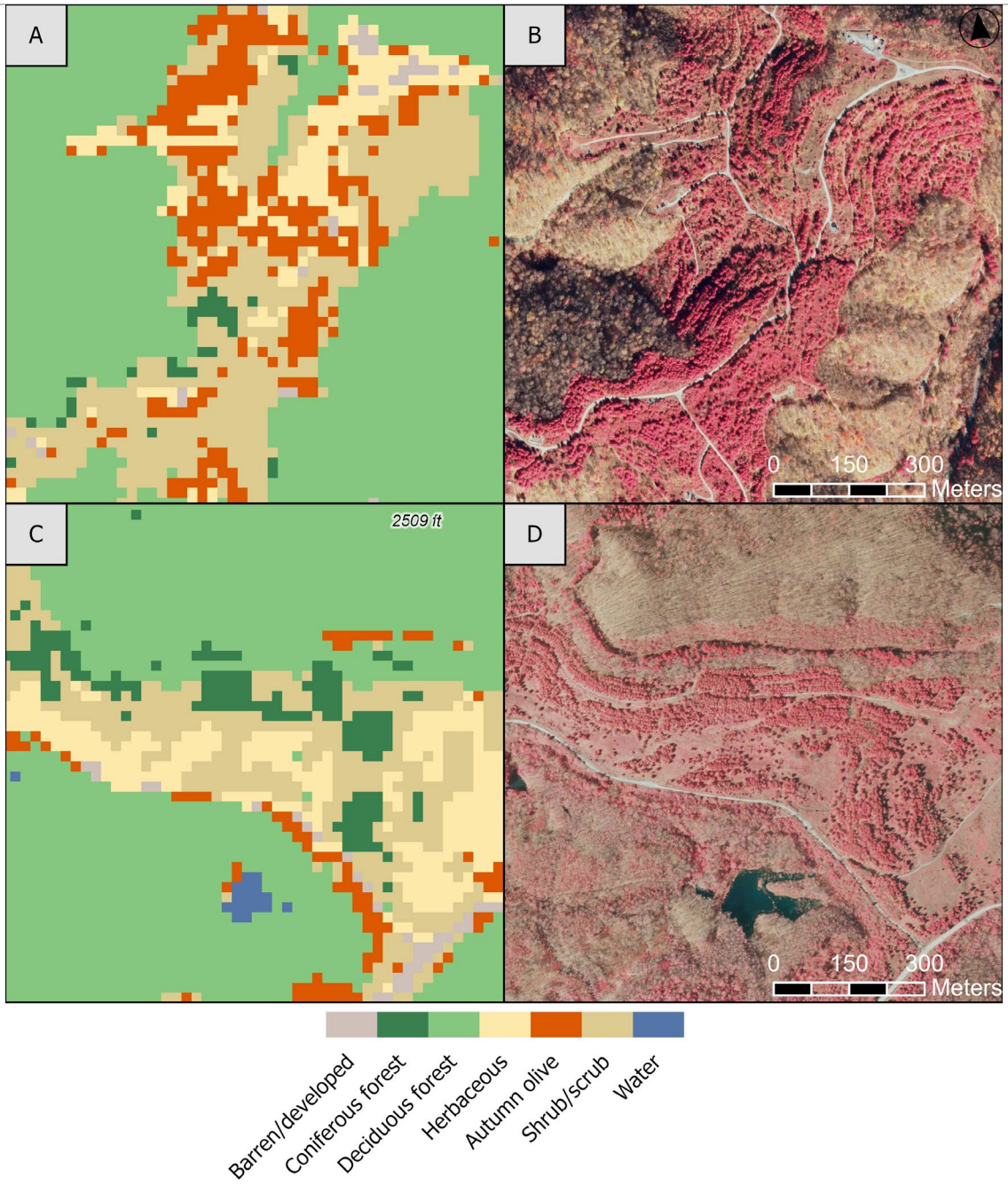


Figure 14: Predicted maps with potential overprediction of the shrub/scrub class, A: Classified land cover data of a mine near Prater Virginia, much of the short conifers are misclassified as shrub/scrub. B: False color NAIP aerial imagery of A. C: Classified land cover data of a mine near Clairfield, Tennessee with many conifers missclassified as shrub/scrub. D: False color NAIP aerial imagery of C.

Progress on stated hypotheses

Hypothesis 1: *A combination of multispectral and height-determining satellite imagery obtained from no-cost sources can be analyzed and interpreted to discriminate the following land-cover types on reclaimed post-SMCRA mines in the Appalachian coalfield with a high degree of accuracy: Sparsely vegetated, managed agriculture, other grasses, autumn olive, shrub/scrub, deciduous forest, coniferous forest, developed, and water.*

> We found that these methods can be used to discriminate these land cover classes, however the overall accuracy for all nine classes was lower than expected. We chose to aggregate these nine classes into a more parsimonious seven class land cover schema. In this new land cover schema, we found that autumn olive and other classes are well detected in Virginia, but accuracy is much lower in Tennessee where autumn olive appears less frequent and more sparse. Generally, accuracy was lower than expected, but not due to a lack of informative classification data. We observed significant landscape heterogeneity and variability in autumn olive density which contributed to misclassifications.

Hypothesis 2: *Plant communities with major components of native deciduous forest trees are more likely to be present on mined lands reclaimed using the Forestry Reclamation Approach (FRA) than on other mined lands of similar ages.*

> We pursued research questions related to the forest characteristics of FRA and non-FRA mine forests. However, after consulting with industry experts, it became clear that the FRA has been so pervasive in this region since its introduction that there are effectively no non-FRA forested mine sites to compare against. There are reports of wide variability in the application of the FRA, which could be an alternative approach to addressing this hypothesis. However, to evaluate the causal relationship between FRA implementation variability and forest characteristic outcomes would require a large number of samples, in varying site conditions, with varying ages, with data on the exact activities conducted relevant to the FRA for each site. We did not have the time or resources to accumulate a dataset to address this question.

Hypothesis 3: *On mined lands not reclaimed using the Forestry Reclamation Approach, plant communities with major components of deciduous forest trees are more likely to be present on:*

1. *Older mines than on younger mined lands;*
2. *Near the edges of mined areas that border native forests than in the interiors of such mined areas;*
3. *On sloping landscapes than on relatively flat landscapes;*
4. *On northern and easter slopes than on southern and western slopes.*

> Again, questions related to the implementation of the FRA is complicated by what we learned from professionals in the field: almost all forests on mines have had some FRA applied, or there would not have been tree planting. However, Figure 8 shows that older mines appear to more closely resemble surrounding vegetation communities with low proportions of barren/developed or autumn olive land and higher proportions of forested and herbaceous land.

Conclusion

This study demonstrates that a novel multi-source approach integrating Sentinel-2 spectral and phenological data, Landsat disturbance metrics, and 3DEP LiDAR structural data can effectively classify complex surface mine land cover in the central Appalachians. By advancing existing methods for autumn olive detection to a multi-class schema, we provided a more comprehensive characterization of the reclamation landscape, achieving area-weighted overall accuracies between 74.3% and 76.8% across two states and three years. The classification results confirm that autumn olive is a significant component of the landscape on Virginia surface mines, covering approximately 9.8% ± 2.7% of Virginia's mined area in 2021. However, the model's inability to accurately detect Autumn olive in Tennessee (F1=0.18), where the species is rare, highlights the limitations of satellite pixel-scale classification, which struggles to identify autumn olive at low densities. Our chronosequence analysis reveals that autumn olive prevalence is temporally dependent, peaking on sites approximately 14 years after initial mining before declining on older sites, suggesting it may eventually be outcompeted by native forest cover in the absence of further disturbance. This classification framework provides a spatially extendable and temporally stable method for monitoring reclamation land cover composition, enabling managers and regulators to identify mined areas that fall short of or exceed expectations for desired post-mining land cover.

References

Abrams, M. D. (1992). Fire and the development of oak forests: In eastern North America, oak distribution reflects a variety of ecological paths and disturbance conditions. *BioScience*, *42*(5), 346–353.

Adams, B., Iverson, L., Matthews, S., Peters, M., Prasad, A., & Hix, D. M. (2020). Mapping forest composition with Landsat time series: An evaluation of seasonal composites and harmonic regression. *Remote Sensing*, *12*(4), 610.

Alexander, H. D., Siegert, C., Brewer, J. S., Kreye, J., Lashley, M. A., McDaniel, J. K., Paulson, A. K., Renninger, H. J., & Varner, J. M. (2021). Mesophication of oak landscapes: Evidence, knowledge gaps, and future research. *BioScience*, *71*(5), 531–542.

Anderson, J., Hardy, E., Roach, J., & Witmer, R. (1976). *A land use and land cover classification system for use with remote sensor data* (Professional Paper 964). U.S. Geological Survey, U.S. Government Printing Office.

Boyd, D. S., Sanchez-Hernandez, C., & Foody, G. M. (2006). Mapping a specific class for priority habitats monitoring from satellite sensor data. *International Journal of Remote Sensing*, *27*(13), 2631–2644.

Cavender, N., Byrd, S., Bechtoldt, C. L., & Bauman, J. M. (2014). Vegetation communities of a coal reclamation site in southeastern Ohio. *Northeastern Naturalist*, *21*(1), 31–46.

Chance, C. M., Coops, N. C., Plowright, A. A., Tooke, T. R., Christen, A., & Aven, N. (2016). Invasive shrub mapping in an urban environment from hyperspectral and LiDAR-derived attributes. *Frontiers in Plant Science*, *7*.

Chen, W., Li, X., He, H., & Wang, L. (2018). A review of fine-scale land use and land cover classification in open-pit mining areas by remote sensing techniques. *Remote Sensing*, *10*(1), 15.

Choi, D. H., Morton, I. S., Darling, L. E., Wang, J., Thapa, B., Price, E. P. F., Zaya, D. N., Fei, S., & Hardiman, B. S. (2025). Detecting patches of invasive shrubs using high-density airborne LiDAR data and spectral imagery. *Urban Forestry & Urban Greening*, *107*, 128764.

Dewberry. (2018). *Virginia–FEMA R3 Southwest Lidar—2016* (Technical Report G16PD01238). U.S. Geological Survey.

Evans, D. M., Zipper, C. E., Burger, J. A., Strahm, B. D., & Villamagna, A. M. (2013). Reforestation practice for enhancement of ecosystem services on a compacted surface mine: Path toward ecosystem recovery. *Ecological Engineering*, *51*, 16–23.

Evans, J. S., & Hudak, A. T. (2007). A multiscale curvature algorithm for classifying discrete return LiDAR in forested environments. *IEEE Transactions on Geoscience and Remote Sensing*, *45*(4), 1029–1038.

Fagan, M., Morton, D., Cook, B., Masek, J., Zhao, F., Nelson, R., & Huang, C. (2018). Mapping pine plantations in the southeastern U.S. using structural, spectral, and temporal remote sensing data. *Remote Sensing of Environment*, *216*, 415–426.

Foody, G. M. (2002). Status of land cover classification accuracy assessment. *Remote Sensing of Environment*, *80*(1), 185–201.

Fragoso-Campón, L., Quirós, E., Mora, J., Gutiérrez, J. A., & Durán-Barroso, P. (2018). Accuracy enhancement for land cover classification using LiDAR and multitemporal Sentinel 2 images in a forested watershed. *Proceedings*, *2*(20), 1280.

Franke, M. E., Zipper, C., & Barney, J. N. (2018). Native hardwood tree seedling establishment following invasive autumn-olive (*Elaeagnus umbellata*) removal on a reclaimed coal mine. *Invasive Plant Science and Management*, *11*(3), 155–161.

Gorelick, N., Hancher, M., Dixon, M., Ilyushchenko, S., Thau, D., & Moore, R. (2017). Google Earth Engine: Planetary-scale geospatial analysis for everyone. *Remote Sensing of Environment*.

Hartley, F. M., Maxwell, A. E., Landenberger, R. E., & Bortolot, Z. J. (2022). Forest type differentiation using GLAD phenology metrics, land surface parameters, and machine learning. *Geographies*, *2*(3), 491–515.

Hermosilla, T., Wulder, M. A., White, J. C., Coops, N. C., Hobart, G. W., & Campbell, L. B. (2016). Mass data processing of time series Landsat imagery: Pixels to data products for forest monitoring. *International Journal of Digital Earth*, *9*(11), 1035–1054.

Hijmans, R. J. (2025). *terra: Spatial data analysis*.

Jiang, Z., Huete, A. R., Didan, K., & Miura, T. (2008). Development of a two-band enhanced vegetation index without a blue band. *Remote Sensing of Environment*, *112*(10), 3833–3845.

Key, C. H., & Benson, N. C. (2006). Landscape assessment (LA). In D. C. Lutes, R. E. Keane, J. F. Caratti, C. H. Key, N. C. Benson, S. Sutherland, & L. J. Gangi, *FIREMON: Fire effects monitoring and inventory system* (Gen. Tech. Rep. RMRS-GTR-164-CD, pp. LA-1–55). U.S. Department of Agriculture, Forest Service, Rocky Mountain Research Station.

Krawczyk, B., Woźniak, M., & Herrera, F. (2015). On the usefulness of one-class classifier ensembles for decomposition of multi-class problems. *Pattern Recognition*, *48*(12), 3969–3982.

Kuhman, T. R., Pearson, S. M., & Turner, M. G. (2010). Effects of land-use history and the contemporary landscape on non-native plant invasion at local and regional scales in the forest-dominated southern Appalachians. *Landscape Ecology*, *25*(9), 1433–1445.

Liano, X. (2025). *AcATaMa—QGIS plugin for accuracy assessment of thematic maps*.

Loveland, T., Gutman, G., Marilyn, B., Chatterjee, K., Justice, C., Rogers, C., Stokes, B., & Thomas, J. (2003). Land-use/land cover change. In *Strategic plan for the U.S. Climate Change Science Program* (pp. 63–70). Obama White House archives.

Maxwell, A. E., Warner, T. A., Strager, M. P., & Pal, M. (2014). Combining RapidEye satellite imagery and lidar for mapping of mining and mine reclamation. *Photogrammetric Engineering & Remote Sensing*, *80*(2), 179–189.

Maynard-Bean, E., Kaye, M., Wagner, T., & Burkhart, E. P. (2020). Citizen scientists record novel leaf phenology of invasive shrubs in eastern U.S. forests. *Biological Invasions*, *22*(11), 3325–3337.

Morales-Barquero, L., Lyons, M. B., Phinn, S. R., & Roelfsema, C. M. (2019). Trends in remote sensing accuracy assessment approaches in the context of natural resources. *Remote Sensing*, *11*(19), 2305.

Murakami, T., & Tsutsumida, N. (2025). Comparative global assessment and optimization of LandTrendr, CCDC, and BFAST algorithms for enhanced urban land cover change detection using Landsat time series. *Remote Sensing*, *17*(14), 2402.

Næsset, E. (2002). Predicting forest stand characteristics with airborne scanning laser using a practical two-stage procedure and field data. *Remote Sensing of Environment*, *80*(1), 88–99.

Næsset, E., & Gobakken, T. (2005). Estimating forest growth using canopy metrics derived from airborne laser scanner data. *Remote Sensing of Environment*, *96*(3), 453–465.

Nguyen, L. H., Joshi, D. R., Clay, D. E., & Henebry, G. M. (2020). Characterizing land cover/land use from multiple years of Landsat and MODIS time series: A novel approach using land surface phenology modeling and random forest classifier. *Remote Sensing of Environment*, *238*, 111017.

Oliphant, A. J., Wynne, R. H., Zipper, C. E., Ford, W. M., Donovan, P. F., & Li, J. (2017). Autumn olive (*Elaeagnus umbellata*) presence and proliferation on former surface coal mines in eastern USA. *Biological Invasions*, *19*(1), 179–195.

Olofsson, P., Foody, G. M., Herold, M., Stehman, S. V., Woodcock, C. E., & Wulder, M. A. (2014). Good practices for estimating area and assessing accuracy of land change. *Remote Sensing of Environment*, *148*, 42–57.

Oo, T. K., Arunrat, N., Sereenonchai, S., Ussawarujikulchai, A., Chareonwong, U., & Nutmagul, W. (2022). Comparing four machine learning algorithms for land cover classification in gold mining: A case study of Kyaukpahto gold mine, northern Myanmar. *Sustainability*, *14*(17), 10754.

Pasquarella, V. J., Arévalo, P., Bratley, K. H., Bullock, E. L., Gorelick, N., Yang, Z., & Kennedy, R. E. (2022). Demystifying LandTrendr and CCDC temporal segmentation. *International Journal of Applied Earth Observation and Geoinformation*, *110*, 102806.

Pasquarella, V. J., Brown, C. F., Czerwinski, W., & Rucklidge, W. J. (2023). Comprehensive quality assessment of optical satellite imagery using weakly supervised video learning. In *2023 IEEE/CVF Conference on Computer Vision and Pattern Recognition Workshops (CVPRW)* (pp. 2125–2135). IEEE.

Pasquarella, V. J., Holden, C. E., & Woodcock, C. E. (2018). Improved mapping of forest type using spectral-temporal Landsat features. *Remote Sensing of Environment*, *210*, 193–207.

Pedregosa, F., Varoquaux, G., Gramfort, A., Michel, V., Thirion, B., Grisel, O., Blondel, M., Prettenhofer, P., Weiss, R., Dubourg, V., Vanderplas, J., Passos, A., Cournapeau, D., Brucher, M., Perrot, M., & Duchesnay, E. (2011). Scikit-learn: Machine learning in Python. *Journal of Machine Learning Research*, *12*, 2825–2830.

Pham, V.-D., Thiel, F., Frantz, D., Okujeni, A., Schug, F., & Van Der Linden, S. (2024). Learning the variations in annual spectral-temporal metrics to enhance the transferability of regression models for land cover fraction monitoring. *Remote Sensing of Environment*, *308*, 114206.

Pontius Jr., R. G., & Millones, M. (2011). Death to Kappa: Birth of quantity disagreement and allocation disagreement for accuracy assessment. *International Journal of Remote Sensing*, *32*(15), 4407–4429.

Pritekel, C., Whittemore-Olson, A., Snow, N., & Moore, J. C. (2006). Impacts from invasive plant species and their control on the plant community and belowground ecosystem at Rocky Mountain National Park, USA. *Applied Soil Ecology*, *32*(1), 132–141.

QGIS Development Team. (2024). *QGIS Geographic Information System*.

R Core Team. (2021). *R: A language and environment for statistical computing*.

Rouse, J. W., Haas, R. H., Schell, J. A., & Deering, D. W. (1974). *Monitoring vegetation systems in the Great Plains with ERTS* (NTRS Paper No. A20; NTRS Document ID 19740022614). Texas A&M University.

Roussel, J.-R., Auty, D., Coops, N. C., Tompalski, P., Goodbody, T. R. H., Meador, A. S., Bourdon, J.-F., Boissieu, F. d., & Achim, A. (2020). lidR: An R package for analysis of Airborne Laser Scanning (ALS) data. *Remote Sensing of Environment*, *251*, 112061.

Ruggles, T. A., Gerrath, J. A., Ruhm, C. T., Jefferson, A. J., Davis, C. A., & Blackwood, C. B. (2021). Surface mines show little progress towards native species forest restoration following 35 years of passive management after initial reclamation. *Land Degradation & Development*, *32*(7), 2351–2359.

Sasaki, T., Imanishi, J., Ioki, K., Morimoto, Y., & Kitada, K. (2012). Object-based classification of land cover and tree species by integrating airborne LiDAR and high spatial resolution imagery data. *Landscape and Ecological Engineering*, *8*(2), 157–171.

Sena, K., Franklin, J. A., Swab, R. M., & Hall, S. L. (2021). Plant communities on Appalachian mined lands. In C. E. Zipper & J. Skousen (Eds.), *Appalachia's coal mined landscapes: Resources and communities in a new energy era* (pp. 111–134). Springer International Publishing.

Sheridan, R. D., Popescu, S. C., Gatziolis, D., Morgan, C. L. S., & Ku, N.-W. (2015). Modeling forest aboveground biomass and volume using airborne LiDAR metrics and forest inventory and analysis data in the Pacific Northwest. *Remote Sensing*, *7*(1), 229–255.

Shiferaw, H., Bewket, W., & Eckert, S. (2019). Performances of machine learning algorithms for mapping fractional cover of an invasive plant species in a dryland ecosystem. *Ecology and Evolution*, *9*(5), 2562–2574.

Siljander, M., Adero, N., Gitau, F., & Nyambu, E. (2020). *Land use/land cover classification for the iron mining site of Kishushe, Kenya: A feasibility study of traditional and machine learning algorithms*.

Silva, J., Bacao, F., & Caetano, M. (2017). Specific land cover class mapping by semi-supervised weighted support vector machines. *Remote Sensing*, *9*(2), 181.

Skousen, J., & Zipper, C. E. (2021). Coal mining and reclamation in Appalachia. In C. E. Zipper & J. Skousen (Eds.), *Appalachia's coal-mined landscapes: Resources and communities in a new energy era* (pp. 55–83). Springer International Publishing.

Stein, B., Kutner, L., & Adams, J. (2000). *Precious heritage: The status of biodiversity in the United States*. Oxford University Press.

Szostak, M., Pietrzykowski, M., & Likus-Cieślik, J. (2020). Reclaimed area land cover mapping using Sentinel-2 imagery and LiDAR point clouds. *Remote Sensing*, *12*(2), 261.

Thapa, N., Narine, L. L., Fan, Z., Yang, S., & Tiwari, K. (2023). Detection of invasive plants using NAIP imagery and airborne LiDAR in coastal Alabama and Mississippi, USA. *Annals of Forest Research*, *66*(1), 63–77.

Thomas, C. (2023). *Updated MTM data*.

Townsend, P. A., Helmers, D. P., Kingdon, C. C., McNeil, B. E., de Beurs, K. M., & Eshleman, K. N. (2009). Changes in the extent of surface mining and reclamation in the Central Appalachians detected using a 1976–2006 Landsat time series. *Remote Sensing of Environment*, *113*(1), 62–72.

U.S. Congress. (1977). *Surface Mining Control and Reclamation Act*.

Verbesselt, J., Hyndman, R., Zeileis, A., & Culvenor, D. (2010). Phenological change detection while accounting for abrupt and gradual trends in satellite image time series. *Remote Sensing of Environment*, *114*(12), 2970–2980.

Wang, R., Liu, Y., & Liu, X. (2022). Feature selection method for open-pit mine land cover classification based on multi-feature set using Sentinel-2. *Sensors and Materials*, *34*(11), 4017.

Wickham, J. D., Riitters, K. H., Wade, T. G., Coan, M., & Homer, C. (2007). The effect of Appalachian mountaintop mining on interior forest. *Landscape Ecology*, *22*, 179–187.

Wilson, B. T., Knight, J. F., & McRoberts, R. E. (2018). Harmonic regression of Landsat time series for modeling attributes from national forest inventory data. *ISPRS Journal of Photogrammetry and Remote Sensing*, *137*, 29–46.

Woolpert. (2015). *TN 27 county QL2 lidar (Cumberland Plateau)* (Technical Report 75556).

Wu, L., Li, Z., Liu, X., Zhu, L., Tang, Y., Zhang, B., Xu, B., Liu, M., Meng, Y., & Liu, B. (2020). Multi-type forest change detection using BFAST and monthly Landsat time series for monitoring spatiotemporal dynamics of forests in subtropical wetland. *Remote Sensing*, *12*(2), 341.

Xu, P., Tsendbazar, N.-E., Herold, M., de Bruin, S., Koopmans, M., Birch, T., Carter, S., Fritz, S., Lesiv, M., Mazur, E., Pickens, A., Potapov, P., Stolle, F., Tyukavina, A., Van De Kerchove, R., & Zanaga, D. (2024). Comparative validation of recent 10 m-resolution global land cover maps. *Remote Sensing of Environment*, *311*, 114316.

Xue, Z., Du, P., & Feng, L. (2014). Phenology-driven land cover classification and trend analysis based on long-term remote sensing image series. *IEEE Journal of Selected Topics in Applied Earth Observations and Remote Sensing*, *7*(4), 1142–1156.

Yang, L., Jin, S., Danielson, P., Homer, C., Gass, L., Bender, S. M., Case, A., Costello, C., Dewitz, J., Fry, J., Funk, M., Granneman, B., Liknes, G. C., Rigge, M., & Xian, G. (2018). A new generation of the United States National Land Cover Database: Requirements, research priorities, design, and implementation strategies. *ISPRS Journal of Photogrammetry and Remote Sensing*, *146*, 108–123.

Zald, H. S. J., Ohmann, J. L., Roberts, H. M., Gregory, M. J., Henderson, E. B., McGaughey, R. J., & Braaten, J. (2014). Influence of lidar, Landsat imagery, disturbance history, plot location accuracy, and plot size on accuracy of imputation maps of forest composition and structure. *Remote Sensing of Environment*, *143*, 26–38.

Zhang, X., Zhao, T., Xu, H., Liu, W., Wang, J., Chen, X., & Liu, L. (2024). GLC_FCS30D: The first global land-cover dynamics monitoring product with a fine classification system for the period from 1985 to 2022 generated using dense-time-series Landsat imagery and the continuous change-detection method. *Earth System Science Data*, *16*(3), 1353–1381.

Zhu, Z., & Woodcock, C. E. (2014). Continuous change detection and classification of land cover using all available Landsat data. *Remote Sensing of Environment*, *144*, 152–171.

Zipper, C. E. (2020). *Appalachian coal data* [See Table 9].

Zipper, C. E., & Skousen, J. (Eds.). (2021). *Appalachia's coal-mined landscapes: Resources and communities in a new energy era*. Springer International Publishing.

Appendices

Appendix A Vegetation indices used

$$NDVI = \frac{NIR - Red}{NIR + Red} \quad \text{(Eq. A.1)}$$

$$EVI2 = \frac{2.5 * NIR - Red}{NIR + Red + 1} \quad \text{(Eq. A.2)}$$

$$NBR = \frac{NIR - SWIR1}{NIR + SWIR1} \quad \text{(Eq. A.3)}$$

$$NBR2 = \frac{SWIR1 - SWIR2}{SWIR1 + SWIR2} \quad \text{(Eq. A.4)}$$

Appendix B CCDC and disturbance history metrics

Inter-annual variation is represented by the β_0 and β_1 coefficients which correspond to the intercept and slope respectively. Intra-annual change is represented by the β_2 and β_3 coefficients which scale the cos and sin functions respectively. The representation of intra-annual change in the model ranges between 1 and 6 coefficients as a result of the model being parameterized through LASSO regularization. Harmonics are represented in the model as: $\beta_{2,j} \cos\left(\frac{2\pi jt}{T}\right) + \beta_{3,j} \sin\left(\frac{2\pi jt}{T}\right)$ where *j* is the harmonic order, *t* is the Julian date, and *T* is the base period (usually 365 days). As the harmonic order increases, so does the frequency. This means that first order β_2 and β_3 coefficients capture the overall shape within a year and second and third order coefficients add higher frequency patterns. Additionally each segment contains an error term ϵ calculated as the RMSE of the fit within a given segment. The resulting function for a single band, for a given segment bounded by time breakpoints τ_k^* is represented in Equation B.1. This resulted in 48 predictors for the band harmonics, 24 predictors for the vegetation index harmonics, and 36 predictors for the linear fit terms, totaling 108 predictors from the Sentinel-2 CCDC fit.

$$y_t = \beta_0 + \beta_1 t + \sum_{j=1}^{3} \left(\beta_{2,j} \cos\left(\frac{2\pi jt}{T}\right) + \beta_{3,j} \sin\left(\frac{2\pi jt}{T}\right) \right) + \epsilon \quad t \in \{\tau_{k-1}^* < t \leq \tau_k^*\} \quad \text{(Eq. B.1)}$$

Long-term change information from CCDC using Landsat imagery included the number of time series breaks, average segment length, most recent break year, most recent break magnitude (NBR), most recent break age, largest magnitude break year, largest magnitude break magnitude (NBR), largest magnitude break age, and number of years between largest magnitude and most recent breaks.

Appendix C LiDAR parameters and metrics

Land cover height information was processed using the lidR package in R. 3DEP LiDAR tiles were compiled into a LAScatalog and spatially indexed with the catalog laxindex function. LAScatalog parameters set included a 60 m buffer area, a chunk size of 0 (each worker processes one tile at a time). We classified ground points in each tile using multiscale curvature classification and determined parameter values through visual assessment of multiple active mine and reclaimed sites (s = 0.7, t = 0.3). Then we normalized the point cloud heights relative to ground points using the knnidw function with default parameters. Metrics were calculated within 20 m pixels for all points 0.5 m above ground. If a pixel had less than five points above the 0.5 m threshold, all metric values were set to 0. We calculated lidar metrics within three categories: Direct height measurement, distribution of heights, and distribution of returns. Direct height measures include: maximum, minimum, mean, median, and height percentiles: 5, 10, 20, 30, 40, 60, 70, 80, 90, 95, 99. Height distribution metrics included: standard deviation, coefficient of variation, skewness, kurtosis, entropy, proportion of points above ground, and proportion of points falling within five non-overlapping height bin strata (in meters above ground): 0.5 - 2.5, 2.5 - 5.0, 5.0 - 10.0, 10.0 - 20.0, >20. Metrics based on statistical

moments were calculated using the moments package, and entropy was calculated using the included function in lidR. Return distribution metrics included the mean and standard deviation of first returns, and the mean and standard deviation of point return number. In summary, there are 15 height metrics, 11 height distribution metrics, and four return distribution metrics, resulting in 30 Lidar predictors.

Table 7: Selected flight attributes of the USGS 3DEP LiDAR data used to calculate structural characteristics.

Project state	Sensor	Operator	Flight AGL (m)	Max number of returns per pulse	Swath width (m)	Nominal pulse density (ppsm)	Positional RMSE (cm)	Beam diameter (m)
TN	Leica ALS80	Woolpert	1984	4	3325	2.04	5.0	0.45
TN	Leica ALS70	Quantum spatial	1981	7	3325	2.04	5.0	0.44
TN	Leica ALS70	PAR	1798	7	3017	2.04	5.0	0.44
VA	Riegl 680i/780	Leading Edge	1800	7	1996	2.1	6.2	0.40

Appendix D Confusion Matrices for accuracy assessment

Table 8: Post-classification accuracy assessment sample confusion matrix for Virginia 2021.

		Predicted							
		Barren/developed	Coniferous forest	Deciduous forest	Herbaceous	Autumn olive	Shrub/scrub	Water	**Producer's**
Reference	Barren/developed	85	0	3	20	2	2	0	**0.76**
	Coniferous forest	1	73	15	0	1	11	0	**0.72**
	Deciduous forest	6	0	151	1	9	6	0	**0.87**
	Herbaceous	10	0	2	126	10	3	0	**0.83**
	Autumn olive	0	0	1	4	40	3	0	**0.83**
	Shrub/scrub	2	3	3	6	7	17	0	**0.45**
	Water	3	0	3	0	1	0	26	**0.79**
	User's	**0.79**	**0.96**	**0.85**	**0.8**	**0.57**	**0.4**	**1**	**0.79**

Table 9: Post-classification accuracy assessment sample confusion matrix for Virginia 2019.

		Predicted							
		Barren/developed	Coniferous forest	Deciduous forest	Herbaceous	Autumn olive	Shrub/scrub	Water	**Producer's**
Reference	Barren/developed	96	0	2	12	5	1	0	**0.83**
	Coniferous forest	2	68	17	0	1	10	0	**0.69**
	Deciduous forest	6	0	151	3	11	4	0	**0.86**
	Herbaceous	12	0	4	117	17	0	0	**0.78**
	Autumn olive	0	0	0	2	40	0	0	**0.95**
	Shrub/scrub	2	3	3	4	10	13	0	**0.37**
	Water	3	0	3	1	1	1	24	**0.73**
	User's	**0.79**	**0.96**	**0.84**	**0.84**	**0.47**	**0.45**	**1**	**0.78**

Table 10: Post-classification accuracy assessment sample confusion matrix for Virginia 2018.

		Predicted							
		Barren/developed	Coniferous forest	Deciduous forest	Herbaceous	Autumn olive	Shrub/scrub	Water	**Producer's**
Reference	Barren/developed	103	0	3	10	1	0	0	**0.88**
	Coniferous forest	2	68	18	0	2	8	0	**0.69**
	Deciduous forest	10	0	152	4	5	5	0	**0.86**
	Herbaceous	11	0	4	121	8	2	0	**0.83**
	Autumn olive	1	0	2	5	33	1	0	**0.79**
	Shrub/scrub	6	4	3	5	8	12	0	**0.32**
	Water	5	0	3	0	1	0	23	**0.72**
	User's	**0.75**	**0.94**	**0.82**	**0.83**	**0.57**	**0.43**	**1**	**0.79**

Table 11: Post-classification accuracy assessment sample confusion matrix for Tennessee 2021.

		Predicted							
		Barren/developed	Coniferous forest	Deciduous forest	Herbaceous	Autumn olive	Shrub/scrub	Water	**Producer's**
Reference	Barren/developed	71	2	4	19	0	1	1	**0.72**
	Coniferous forest	1	76	3	0	0	15	0	**0.8**
	Deciduous forest	1	0	61	2	17	12	0	**0.66**
	Herbaceous	29	0	4	220	7	3	0	**0.84**
	Autumn olive	0	0	0	2	4	1	0	**0.57**
	Shrub/scrub	0	1	2	15	9	11	0	**0.29**
	Water	3	0	1	2	0	0	33	**0.85**
	User's	**0.68**	**0.96**	**0.81**	**0.85**	**0.11**	**0.26**	**0.97**	**0.75**

Table 12: Post-classification accuracy assessment sample confusion matrix for Tennessee 2019.

		Predicted							
		Barren/developed	Coniferous forest	Deciduous forest	Herbaceous	Autumn olive	Shrub/scrub	Water	**Producer's**
Reference	Barren/developed	81	0	1	29	0	2	1	**0.71**
	Coniferous forest	2	91	2	1	0	15	0	**0.82**
	Deciduous forest	2	0	69	3	16	10	0	**0.69**
	Herbaceous	22	0	0	194	9	1	0	**0.86**
	Autumn olive	0	0	0	1	6	0	0	**0.86**
	Shrub/scrub	1	6	2	9	7	8	0	**0.24**
	Water	4	0	2	0	0	0	33	**0.85**
	User's	**0.72**	**0.94**	**0.91**	**0.82**	**0.16**	**0.22**	**0.97**	**0.77**